Binary black holes population and cosmology in new lights: Signature of PISN mass and formation channel in GWTC-3

Christos Karathanasis, Suvodip Mukherjee, Simone Mastrogiovanni

▶ **To cite this version:**

Christos Karathanasis, Suvodip Mukherjee, Simone Mastrogiovanni. Binary black holes population and cosmology in new lights: Signature of PISN mass and formation channel in GWTC-3. Mon.Not.Roy.Astron.Soc., 2023, 523 (3), pp.4539-4555. 10.1093/mnras/stad1373 . hal-03665439

HAL Id: hal-03665439
https://hal.science/hal-03665439v1

Submitted on 6 Sep 2024

HAL is a multi-disciplinary open access archive for the deposit and dissemination of scientific research documents, whether they are published or not. The documents may come from teaching and research institutions in France or abroad, or from public or private research centers.

L'archive ouverte pluridisciplinaire **HAL**, est destinée au dépôt et à la diffusion de documents scientifiques de niveau recherche, publiés ou non, émanant des établissements d'enseignement et de recherche français ou étrangers, des laboratoires publics ou privés.

Distributed under a Creative Commons Attribution 4.0 International License

Monthly Notices of the ROYAL ASTRONOMICAL SOCIETY

MNRAS **523,** 4539–4555 (2023) https://doi.org/10.1093/mnras/stad1373

Binary black holes population and cosmology in new lights: signature of PISN mass and formation channel in GWTC-3

Christos Karathanasis [1], Suvodip Mukherjee [2,3]★ and Simone Mastrogiovanni [4]

[1] *Institut de Física d'Altes Energies (IFAE), Barcelona Institute of Science and Technology, E-08193 Barcelona, Spain*
[2] *Perimeter Institute for Theoretical Physics, 31 Caroline Street N., Waterloo, Ontario, N2L 2Y5, Canada*
[3] *Department of Astronomy & Astrophysics, Tata Institute of Fundamental Research, 1, Homi Bhabha Road, Colaba, Mumbai 400005, India*
[4] *Artemis, Université Côte d'Azur, Observatoire de la Côte d'Azur, CNRS, F-06304 Nice, France*

Accepted 2023 April 30. Received 2023 April 25; in original form 2022 May 3

ABSTRACT

The mass, spin, and merger rate distribution of the binary black holes (BBHs) across cosmic redshifts provide a unique way to shed light on their formation channel. Along with the redshift dependence of the BBH merger rate, the mass distribution of BBHs can also exhibit redshift dependence due to different formation channels and dependence on the metallicity of the parent stars. We explore the redshift dependence of the BBH mass distribution jointly with the merger rate evolution from the third gravitational wave (GW) catalogue GWTC-3 of the LIGO–Virgo–KAGRA collaboration. We study possible connections between peak-like features in the mass spectrum of BBHs and processes related to supernovae physics and time delay distributions. We obtain a preference for short-time delays between star formation and BBH mergers. Using a power-law form for the time delay distribution ($(t_d^{\rm min})^d$), we find $d < -0.7$ credible at 90 per cent interval. The mass distribution of the BBHs could be fitted with a power-law form with a redshift-dependent peak feature that can be linked to the pair instability supernovae (PISN) mass-scale $M_{\rm PISN}(Z_*)$ at a stellar metallicity Z_*. For a fiducial value of the stellar metallicity $Z_* = 10^{-4}$, we find the $\rm M_{PISN}(Z_*) = 44.4^{+7.9}_{-6.3}M_\odot$. This is in accordance with the theoretical prediction of the lower edge of the PISN mass-scale and differs from previous analyses. Although we find a strong dependence of the PISN value on metallicity, the model that we explored is not strongly favoured over those that do not account for metallicity as the Bayes factors are inconclusive. In the future with more data, evidence towards metallicity dependence of the PISN will have a significant impact on our understanding of stellar physics.

Key words: gravitational waves – black hole mergers – cosmology: miscellaneous.

1 INTRODUCTION

Gravitational wave (GW) observations bring a wealth of information to a broad range of topics ranging from astrophysics, cosmology, and fundamental physics. The first GW detection (Abbott et al. 2016b) opened a new way of observing the Universe. The latest measurements from the LIGO-Virgo-KAGRA (LVK)(Gregory 2010; Aso et al. 2013; Acernese et al. 2014; Aasi et al. 2015; Abbott et al. 2016a, 2018; Tse et al. 2019; Akutsu et al. 2021; Abbott et al. 2021a) have detected 90 compact objects that are constituents of binary neutron stars (BNSs), neutron star binary black holes (NSBHs), and binary black holes (BBHs) (Abbott et al. 2021b). The observed GW sources give a direct probe to infer the mass distribution of compact objects across a range of cosmic redshifts. The recent measurement by the LVK collaboration exhibit that the mass distribution of BBHs shows a power-law + Gaussian (PLG) distribution (Abbott et al. 2019b, 2021b,c,d,e). Along with the mass distribution, a power-law model of the BBHs merger rate is inferred from LVK analysis (Abbott et al. 2019a, 2021b,c,e,h). The mass distribution of GW sources and the merger rate provides a direct way to understand the formation channel of BBHs if an underlying physical model can be inferred from observations.

The currently used phenomenological PLG model of mass distribution does not consider redshift evolution. However, the mass distribution of astrophysical BBHs is likely to exhibit a redshift dependence due to the dependence of the black hole masses on stellar properties, such as the stellar metallicity (Bethe & Brown 1998; Portegies Zwart & Yungelson 1998; Belczynski, Kalogera & Bulik 2002; Heger & Woosley 2002; Dominik et al. 2012; Dominik et al. 2015; Mapelli et al. 2017; Spera & Mapelli 2017; Giacobbo, Mapelli & Spera 2018; Toffano et al. 2019; Farmer et al. 2019a; Renzo et al. 2020; Baxter et al. 2021; Mehta et al. 2022). One of the inevitable ways the BBHs distribution can get a complex redshift dependence is through a time delay acting between the binary formation and the merger. (Mukherjee 2022). This delay causes the population of BBHs at a given redshift to encode information of astrophysical processes and channels that were present at a different cosmic epoch. The time delay contribution will produce a BBH population at a merger redshift z (that is non-trivial to describe with simple models) which is composed by black holes formed at different cosmic times with possibly different astrophysical formation channels. The time delay distribution and the dependence of the astrophysical processes on cosmic time can lead to a non-trivial BBH merger mass spectrum.

The mass distribution of BBHs can also play an important role in inferring the cosmic expansion history (Taylor, Gair & Mandel 2012; Farr et al. 2019; You et al. 2021; Mastrogiovanni et al.

★ E-mail: suvomu@gmail.com

© 2023 The Author(s)
Published by Oxford University Press on behalf of Royal Astronomical Society

Downloaded from https://academic.oup.com/mnras/article/523/3/4539/7204644 by guest on 06 September 2024

2021a; Ezquiaga & Holz 2022; Leyde et al. 2022; Mancarella, Genoud-Prachex & Maggiore 2022; Mukherjee 2022). As the masses of the GW sources are redshifted ($m^{\rm det} = (1 + z)m$), one can expect to infer the redshift from the mass distribution of the GW sources, if the mass distribution of the BBHs can exhibit a universal property or at least a standardized behaviour. We can break the mass-redshift degeneracy and infer the cosmic expansion history from dark standard sirens without applying the cross-correlation technique (Oguri 2016; Mukherjee & Wandelt 2018; Bera et al. 2020; Mukherjee, Wandelt & Silk 2020; Scelfo et al. 2020; Cañas-Herrera, Contigiani & Vardanyan 2021; Mukherjee et al. 2021a; Mukherjee, Wandelt & Silk 2021b; Cigarrán Díaz & Mukherjee 2022; Mukherjee et al. 2022; Scelfo et al. 2022) or statistical host identification technique (Schutz 1986; MacLeod & Hogan 2008; Del Pozzo 2012; Arabsalmani, Sahni & Saini 2013; Fishbach et al. 2019; Soares-Santos et al. 2019; Gray et al. 2020; Abbott et al. 2020b; 2021g; Finke et al. 2021; Palmese et al. 2023;). However, if BBH mass distribution exhibits redshift dependence due to its intrinsic dependence on the delay time distribution, then cosmic redshifts cannot be accurately inferred (Ezquiaga & Holz 2022; Mukherjee 2022), and it can bias the results if the redshift dependence of the mass distribution is not considered. Exploring the merger rate distribution to explore cosmology from dark sirens is also studied for the third-generation GW detectors (Ding et al. 2019; Ye & Fishbach 2021; Leandro, Marra & Sturani 2022).

In this paper, we make a first joint estimation of the BBH merger rate evolution, mass distribution, and metallicity dependance parameters by allowing for the redshift dependence of the BBH mass distribution and H_0. This measurement makes it possible to also infer the delay time distribution of the BBHs in a consistent framework along with the cosmological parameters. The paper is organized as follows, In Section 2.1, we discuss the redshift dependence of the mass distribution of the BBHs and its merger rate. In Section 3 and Section 4, we discuss the basic Bayesian framework used in this analysis, the results from the joint estimation, and we compare these results with the results inferred by the LVK collaboration. Finally, we conclude the analysis of this work and future prospects in Section 5.

2 MODELLING REDSHIFT DEPENDENCE OF THE BBH SOURCE POPULATION

In this analysis, we use the following model to describe the distribution of BBHs in terms of their source frame masses m_1, m_2, and merger redshift z_m:

$$p(m_1, m_2, z_m|\Phi) = p(m_1, m_2|z_m, \Phi_m, \Phi_d, \Phi_{\rm nuis})p(z_m|\Phi_d, \Phi_c), \quad (1)$$

where $\Phi = \{\Phi_{\rm m}, \Phi_{\rm c}, \Phi_{\rm d}, \Phi_{\rm nuis}\}$ are a set of population parameters governing the mass model ($\Phi_{\rm m}$), cosmology ($\Phi_{\rm c}$), time delay ($\Phi_{\rm d}$), and a set of nuisance parameters ($\Phi_{\rm nius}$). In the following section, we explain in detail each of those terms individually.

2.1 The redshift dependence of the mass distribution: mixing of black holes

The distribution of BBHs observed by LVK spans a range of redshift and masses that is currently modelled using different phenomenological models out of which the PLG model fits the data the best (Abbott et al. 2019b, 2021b,c, d, e) but does not explore the redshift dependence of the BBH mass distribution. In this paper, we explore how an astrophysically motivated mass distribution of the BBHs originating due to the effect of the *time delay distribution* agrees with the GWTC-3 data. The observed mass distribution of the BBHs is driven by the underlying astrophysical properties of the parent stars of the individual black hole and the mixing of black holes formed in different redshifts, both of which lead to a redshift dependence of the observed BBH mass distribution.

The redshift dependence of the observed BBH mass distribution in the mixing of BBH model, which we consider in this analysis, is due to three effects, (i) metallicity dependence of the pair-instability supernovae (PISN) mass-scale, (ii) redshift evolution of the stellar metallicity, (iii) distribution of delay times between the formation of the stars that will later become BHs, and for them to merge with another black hole. We will briefly describe below all these aspects.

(i) According to the PISN process, the mass distribution of BHs is expected to feature a mass gap due to the mass loss of heavy stars (Spera & Mapelli 2017; Farmer et al. 2019a; Renzo et al. 2020). The mass loss during the PISN sets the lower limit of the mass gap at around $M_{PISN} = 45\,{\rm M}_\odot$. However, $M_{\rm PISN}$ is also closely related to the stellar metallicity. It was shown (Spera & Mapelli 2017; Farmer et al. 2019a; Renzo et al. 2020) that $M_{\rm PISN}$ varies less than 10 per cent for a variation of the stellar metallicity Z from 10^{-5} to 3×10^{-3} from a 1-D stellar evolution model Modules for Experiments in Stellar Astrophysics (MESA) (Paxton et al. 2011, 2019). The stars with higher metallicity have a larger mass loss due to stellar winds, which leads to a lower value of the PISN mass-scale, than stars formed with lower metallicity. As a result, the position of the $M_{\rm PISN}$ will vary. Given the simplicity of current modeling of stellar winds in 1-D codes such as MESA and the lack of independent observations to determine the PISN mass-scale, the dependence of $M_{\rm PISN}$ on stellar properties is still subject to large uncertainties.

(ii) The metallicity in the Universe varies with redshift and also with the individual galaxies. The global evolution of the stellar metallicity (Belczynski et al. 2002; Dominik et al. 2012; Dominik et al. 2015; Mapelli et al. 2017; Giacobbo et al. 2018; Safarzadeh & Farr 2019; Toffano et al. 2019) indicates that the Universe at high redshift has poor stellar metallicity than at low redshift. As a result, the BHs formed at high redshift may have a higher PISN mass-scale than the BHs formed at low.

(iii) Finally, the BHs that we observe using GWs are not the individual BHs, but binaries. Though the formation of a black hole takes only a few Myrs, a black hole requires much more time to form a binary and merge. As a result, there is a non-zero delay time between the formation of a star and the merging of BHs. This delay time depends on the formation channels of the BBHs (Banerjee, Baumgardt & Kroupa 2010; O'Shaughnessy, Kalogera & Belczynski 2010; Dominik et al. 2012; Dominik et al. 2015; Lamberts et al. 2016; Mandel & de Mink 2016; Cao, Lu & Zhao 2018; Elbert, Bullock & Kaplinghat 2018; Eldridge, Stanway & Tang 2019; Vitale et al. 2019; du Buisson et al. 2020; Santoliquido et al. 2021). Moreover, the delay time is not a fixed number for all the BHs, but rather it follows a distribution that is expected to be a power law from simulations. For a flat in the log-space distribution of the separation of the BHs, the delay time distribution is going to be t_d^{-1} with a minimum delay time from a few hundreds of Myrs to a few Gyrs, depending on the formation channels. The current constraints from GWTC-2 (Fishbach & Kalogera 2021) and the stochastic GW background (Mukherjee & Silk 2021) are weak. In the future, data-driven measurement is possible by combining GW sources with emission line signal (Mukherjee & Dizgah 2022). Consequently, by combining these three effects, we can expect that the observed BHs detected in a binary system are going to have a redshift-dependent mass distribution due to a phenomena of mixing of BHs.

Downloaded from https://academic.oup.com/mnras/article/523/3/4539/7204644 by guest on 06 September 2024

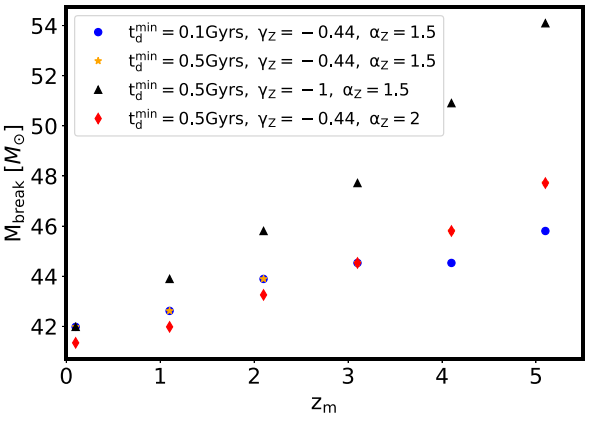

Figure 1. The position of the $M_{\rm break}$ as a function of redshift varying different parameters. The plot was created with fixed $d = -1, H_0 = 70$ km/s/Mpc, and $\Omega_m = 0.3$. Varying d does not affect the position of $M_{\rm break}$.

Origin of the redshift dependence of black hole masses: Following the analysis that was presented in Mukherjee (2022), the mass distribution of BHs at a merging redshift z_m is given by

$$p(m_1|z_m, \Phi_{m_1}, \Phi_d, \Phi_{nuis}) = p(m_1|z_m, \Phi_{m_1}) W_{t_d}(m_1; z_m|\Phi_{nuis}), \quad (2)$$

where m_1 is the most massive BH mass in the source frame, $p(m_1|z_m, \Phi_{m_1})$ is a BH mass distribution which can be associated with the initial mass function (IMF) and $W_{t_d}(m; z_m)$ is the window function that takes into account the delay time of the mergers (Mukherjee et al. 2021c). The BH mass model used in this analysis is described in detail later in equation (10). The window function given in equation (2) is calculated using

$$W_{t_d}(m; z_m) = N \int_{z_m}^{\infty} P_t(t_d|t_d^{min}, t_d^{\rm max}, d) \frac{dt}{dz_f} W(m; z_f) dz_f, \quad (3)$$

where N is a normalization factor, $P_t(t_d|t_d^{min}, t_d^{\rm max}, d)$ is the delay time distribution, $W(m; z_f)$ is a Heaviside step function $W(m; z_f) = \Theta(M_{\rm PISN}(z_f) - m)$, and z_f is the redshift of the formation of a black hole, which puts a cut-off up to a mass of $M_{\rm PISN}$. The delay time distribution is taken to be a simple power-law function of the delay time t_d:

$$P_t(t_d|t_d^{min}, t_d^{\rm max}, d) \propto \begin{cases} (t_d)^d & \text{, for } t_d^{min} < t_d < t_d^{\rm max} \\ 0 & \text{, otherwise} \end{cases}, \quad (4)$$

and the delay time is given by $t_d = t_m - t_f$, with the notation $t_m = t(z_m)$, $t_f = t(z_f)$ to be the time of merger and time of formation, respectively. The $W_{t_d}(m; z_m)$ function brings a breaking point $M_{\rm break}$ at the mass distribution, after which the mass distribution is suppressed depending on the form of the delay time distribution, the dependence of the PISN mass-scale on stellar metallicity, and the redshift evolution of the stellar metallicity. It is evaluated from the combination of different $M_{\rm PISN}$ values that are governed by the minimum delay time $t_{\rm d}^{\rm min}$, metallicity evolution $\gamma_{\rm Z}$, and dependence of PISN mass-scale on metallicity $\alpha_{\rm Z}$. The evolution of the $M_{\rm break}$ for different choices of these parameters can be seen in Fig. 1. At a given z_m, the value of $M_{\rm break}(z_m)$ is the minimum of PISN over the formation redshifts included in $z(z_m, t_d^{\rm min}) < z_f < z(z_m, t_d^{\rm max})$, namely

$$M_{\rm break}(z_m) = \min_{t_d \in [t_d^{\rm min}, t_d^{\rm max}]} M_{\rm PISN}(z_f(t_d, z_m)). \quad (5)$$

Assuming the dependence of the PISN mass-scale on metallicity $M_{\rm PISN}(Z)$ studied by Spera & Mapelli (2017), Farmer et al. (2019a), and Renzo et al. (2020) can be reliably scaled using a parameter $\alpha_{\rm Z}$ (Mukherjee 2022), we can then model it with metalicity as follows:

$$M_{\rm PISN}(Z) = M_{\rm PISN}(Z_*) - \alpha_{\rm Z} \log_{10}(Z/Z_*), \quad (6)$$

and for a power-law redshift evolution of the stellar metallicity (as supported by the current observations (Mannucci et al. 2010; Krumholz & Dekel 2012; Sommariva et al. 2012; Dayal, Ferrara & Dunlop 2013; Madau & Dickinson 2014)), we can write the redshift dependence of metallicity as $\log Z(z) = \gamma_{\rm Z} z + \zeta$. Consequently, the previous equation can be written as follows:

$$M_{\rm PISN}(z) = M_{\rm PISN}(Z_*) - \alpha_{\rm Z}[\gamma_{\rm Z} z + \zeta - \log_{10}(Z_*)], \quad (7)$$

where $\zeta = 10^{-2}$ is taken to be a constant to match the low-redshift measurement of the stellar metallicity $Z(z = 0) \approx 10^{-2}$ and $Z_* = 10^{-4}$. We select this Z_* value as it is a mid-value inside the range for which PISN dependence has been explored in 1-D stellar mass model (Farmer et al. 2019a). In our analysis, we sample for the value of $M_{\rm PISN}(Z_*)$.

The above expression is written in terms of the global evolution of stellar metallicity with redshift. However, at any particular redshift, there is going to be additional variation in the stellar metallicity depending on the property of the host galaxy. So, we would expect variation in the parameter $\gamma_{\rm Z}$ on the property of the host galaxy. However, currently, due to the poor sky location error of the GW sources, we cannot identify the host galaxy and hence cannot model the parameter $\gamma_{\rm Z}$ as a function of the galaxy. As a result, there can be an additional variation in the $\gamma_{\rm Z}$ that cannot be well-modelled currently. Similarly, the parameter $\alpha_{\rm Z}$ controls the dependence of the PISN mass-scale on the metallicity (Farmer et al. 2019a). Hence we treat both these parameters as nuisance parameters in this analysis. We choose wide priors on $\alpha_{\rm Z}$, $\gamma_{\rm Z,}$ which broadly include expected values from works cited above.

The connection of the observed BBH mass distribution with the PISN mass-scale: We model the distribution of BBHs in terms of their source frame masses m_1, m_2 (with $m_1 \geq m_2$), and merger redshift z_m of the binary as follows:

$$p(m_1, m_2|z_m, \Phi_m, \Phi_d, \Phi_{nuis}) = p(m_1|z_m, \Phi_{m_1}, \Phi_d, \Phi_{nuis}) p(m_2|.m_{.1}, \Phi_{m_2}) S_1 S_2. \quad (8)$$

The masses in the detector frame (or redshifted masses) are given by:

$$m^{det} = (1 + z_m)m, \quad (9)$$

where m are the masses in the source frame. To capture the mass distribution of BBHs that originate from the BH mass distribution of equation (2), we consider $p(m_1|z_m, \Phi_{m_1})$ to be given by a power-law distribution superpositioned with the distribution of a Gaussian peak (Talbot & Thrane 2018; Abbott et al. 2021b,d,h):

$$p(m_1|z_m, \Phi_{m_1}) = (1 - \lambda_g) P(m_1|.m_{.\rm min}, M_{\rm max}, -\alpha) + \lambda_g G(m_1|.m_{.\rm break}(z_m), \sigma_g), \quad (10)$$

where $\Phi_{m_1} = \{M_{\rm min}, M_{\rm max}, \alpha, \lambda_g, M_{\rm break}(z_m), \sigma_g\}$, $G(m_1|.m_{.\rm break}(z_m), \sigma_g)$ is a Gaussian distribution with $\mu = M_{\rm break}(z_m)$ and $\sigma = \sigma_g$ and $P(m_1|.m_{.\rm min}, M_{\rm max}, -\alpha)$ is a power-law distribution with slope $-\alpha$ between $M_{\rm min}$ and $M_{\rm max}$. In this model, the power-law part of the mass distribution is motivated by the power-law form of the initial mass function (IMF) Kroupa (2002) and the Gaussian part of the mass distribution is motivated by the PISN mass-scale. The sources merging at redshift z_m due to the contribution from all the higher redshift will lead to an excess near

Downloaded from https://academic.oup.com/mnras/article/523/3/4539/7204644 by guest on 06 September 2024

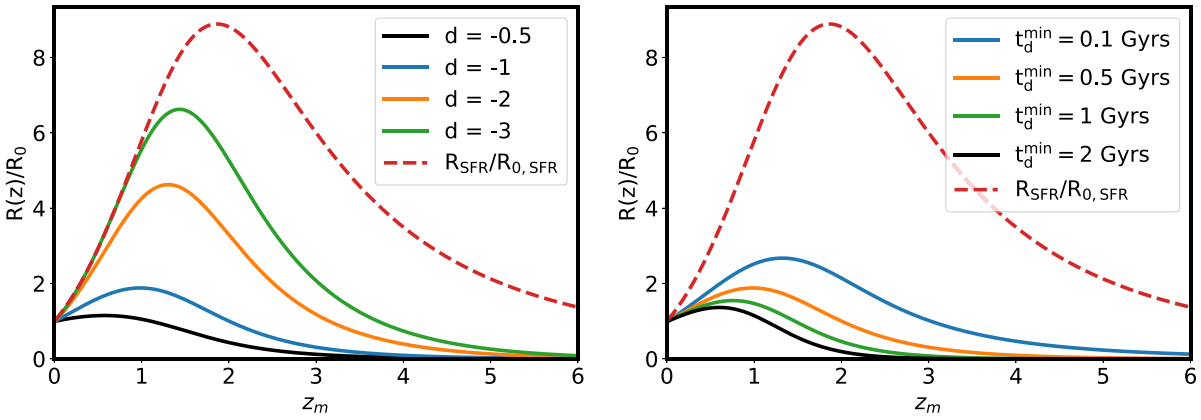

Figure 2. The merger rate function $R(z)/R_0$ for various values of the parameters d, $t_d^{\rm min}$, and fiducial flat Cold Dark Matter cosmology with a constant energy density for dark energy, $H_0 = 70$ km/s/Mpc and $\Omega_m = 0.3$. Left: Fixing $t_d^{\rm min} = 0.5$ Gyrs and varying d. Right: Fixing $d = -1$ and varying $t_d^{\rm min}$. On the plots, the star formation rate $R_{SFR}/R_{0,\,SFR}$ can also be seen.

the value of $M_{\rm break}$ and then a decline in the mass distribution due to the window function. The position of the Gaussian peak μ is considered at the break of the window function at that redshift, which depends on the metallicity dependence of the PISN mass-scale and delays time distribution. The value of the PISN mass-scale is inferred for the metallicity value at $Z_* = 10^{-4}$ (for which the results are obtained by Farmer et al. (2019b)). The Gaussian peak modelled in this analysis gets a physical motivation expected from the PISN mass-scale but is also expected to evolve as a function of the redshift of BBHs mergers.

The distribution of m_2 in the source frame is considered to be given by a power law with maximum value m_1:

$$p(m_2|\Phi_{m_2}) = P(m_2|.m_{.\rm min}, m_1, \beta). \tag{11}$$

Since m_2 is conditional to m_1, the window function W_{t_d} is being applied also to m_2 indirectly.

Finally, the functions $S_{(1,\,2)} = S(m_{(1,\,2)}|\delta_m, M_{\rm min})$ are sigmoid-like window functions to smooth the lower end of the distributions (see appendix A of Abbott et al. (2021d)). We choose to consider only the position of the Gaussian peak to vary with redshift since this is the most prominent feature in the mass spectrum of BHs and is the best-constrained parameter. Other mass parameters of the mass model ($M_{\rm max}$, α, $M_{\rm min}$,...) can also be given a redshift or metallicity dependence (van Son et al. 2022). However, currently, with the limited number of GW sources, measurement of the redshift dependence of the additional parameters will be difficult or unlikely to be strongly constraining.

2.2 The redshift dependence of the BBH merger rate distribution

The distribution $p(z_m|\Phi_d, \Phi_c)$ takes into account the BBH merger rate as a function of redshift and it is built as follows:

$$p(z_m|\Phi_d, \Phi_c) = C\,\frac{R(z_m)}{1+z}\,\frac{dV_c}{dz_m}|_{\Phi_c}, \tag{12}$$

where C is a normalization constant, $\frac{dV_c}{dz_m}$ the differential of the comoving volume, and $R(z_m)$ the BBH merger rate as function of redshift. The BBH merger rate is built as follows:

$$R(z_m) = R_0\,\frac{\int_{z_m}^{\infty} P_t(t_d|t_d^{min}, t_d^{\rm max}, d) R_{SFR}(z_f)\frac{dt}{dz_f}dz_f}{\int_0^{\infty} P_t(t_d|t_d^{min}, t_d^{\rm max}, d) R_{SFR}(z_f)\frac{dt}{dz_f}dz_f}, \tag{13}$$

where z_f is the redshift of formation, R_0 the BBH merger rate today, $P_t(t_d|t_d^{min}, t_d^{\rm max}, d)$ is a time delay distribution between formation and merger of the binary and $R_{SFR}(z_f)$ is a parametrization for the Madau–Dickinson star formation rate (SFR) (Madau & Dickinson 2014).

We show the BBH merger rate for a few values of the variables d, $t_d^{\rm min}$, and a fiducial flat Lambda Cold Dark Matter (LCDM) cosmology model with $H_0 = 70$ km/s/Mpc and $\Omega_m = 0.3$ in Fig. 2 with $R_0 = 20$ Gpc^{-3} yr^{-1}. The plot indicates that with the decrease in the value of power-law index d and minimum delay time $t_d^{\rm min}$, the peak in the BBH merger shifts towards a higher redshift with a steeper slope at low redshift. Current observations from LVK can measure BBHs at redshifts ($z < 1$) (for a fiducial model of cosmology).

The above discussion shows that the delay time distribution $P_t(t_d|t_d^{min}, t_d^{\rm max}, d)$ plays a role in both the mass distribution of the BHs and also in their merger rates. As a result, to infer the BBH formation channel and the delay time distribution, it will be necessary to use both merger rate and mass distribution to infer the delay time distribution of BBHs. Moreover, to estimate the redshift of the BHs from their mass distribution, one needs to account for the redshift dependence of the BBH mass distribution. As a result, we need to conjointly infer the cosmological parameters along with the delay time distribution of BHs, and the black hole mass distribution, to correctly marginalize the degenerate parameters.

3 BAYESIAN FRAMEWORK TO INFER COSMOLOGY FROM GW POPULATION

We construct a Bayesian model following the method described in Mastrogiovanni et al. (2021b) and Abbott et al. (2021d) to conjointly infer the redshift dependence of the mass distribution and merger rate along with the cosmological parameters. In Fig. 3, we show a schematic diagram explaining the formalism. As a cosmological model, we consider a flat LCDM (Planck Collaboration VI 2018). Given a set of N GW detections associated with the data $\{x\} = (x_1,..., x_N)$, the posterior on Φ can be expressed as (Mandel, Farr & Gair 2019; Thrane & Talbot 2019; Vitale et al. 2021; Mastrogiovanni et al. 2021b; Abbott et al. 2021d)

$$p(\Phi, \{x\}, N) = \Pi(\Phi) e^{-N_{\rm exp}(\Phi)} N_{\rm exp}(\Phi)^{N_{\rm obs}} \times \prod_{i=1}^{N} \frac{\int p(x_i|\Phi, \theta) p_{\rm pop}(\theta|\Phi) d\theta}{\int p_{\rm det}(\Phi, \theta) p_{\rm pop}(\theta|\Phi) d\theta}, \tag{14}$$

Downloaded from https://academic.oup.com/mnras/article/523/3/4539/7204644 by guest on 06 September 2024

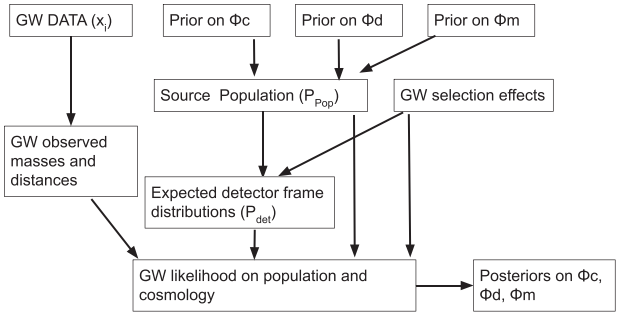

Figure 3. Flow chart of the inference method.

where $\Pi(\Phi)$ is prior on the parameters, θ is the set of intrinsic parameters, which are unique for each event, $p(x_i|\Phi, \theta)$ is the likelihood, $p_{det}(\theta, \Phi)$ is the probability of detection and $p_{pop}(\theta|\Phi)$ is the population modelled prior. Finally, $N_{\rm exp}(\Phi)$ is the expected number of detections in a given observing time and $N_{\rm obs}$ is the number of events considered in the analysis. The term $p_{pop}(\theta|\Phi)$ is given by equation (1). This term captures the effects of delay time between formation and merger.

The denominator of equation (14) normalizes the numerator and takes into account the selection effects (Mastrogiovanni et al. 2021b; Abbott et al. 2021d). It is written as an integral over all detectors' data that pass certain detection criteria for given known noise properties of the detectors. The term $p_{det}(\theta, \Phi)$ is the probability of detecting the source with parameters θ and assuming hyper-parameters Φ.

The summary of the priors used for the parameters that we consider in our model can be found in Table 1.

4 RESULTS FROM GWTC-3

We analysed all the BBH events from GWTC-3 (Abbott et al. 2021c) with the matched-filtering signal-to-noise ratio (SNR) in at least one of the detection pipelines higher than 12. We select a high SNR threshold to avoid any possible contamination from noise. Moreover, the choice of a high SNR threshold is motivated by the fact that our selection biases are evaluated with injections in simulated and not real data. Detection properties between simulated data and real data might be different, especially when lowering the threshold for detection. For all the events, we also require a false alarm rate $< 0.25\,{\rm yr}^{-1}$.

The injection campaign is done in simulated data with duration and sensitivity typical of O1, O2, and O3. For all the observing runs, we assume independent duty cycles among the LIGO Hanford (H1), LIGO Livingston (L1), and Virgo (V1) detectors taken from Abbott et al. (2021f) for O1, O2, and O3 (Buikema et al. 2020; The LIGO Scientific Collaboration et al. 2023). For O1, we assume duty cycles of 64.6 per cent for H1 and 57.4 per cent for L1, while in O2 it was 65.3 per cent and 61.8 per cent. For the entire O3, we assumed 74.6 per cent for H1, 77.0 per cent for L1, and 76.0 per cent for V1. We used the power spectral density of the publicly available detectors for O1[1] and O2[2], while for O3 we used an estimation provided with the first 3 months of O3.[3] Moreover, we have assumed the noise of the detector to be Gaussian and stationary. The injections are performed using the IMRPHENOMPV2 waveform model and are drawn from a distribution in detector frame masses and luminosity distance large enough to cover all the detectable sources assuming a Gaussian stationary detector noise. The mass and luminosity distance distributions of the GWTC-3 catalogue for sources with SNR $\geq$ 12 can be seen in Fig. 4. For the results in this section, we do not consider GW190521, as it is expected to belong to second-generation BHs (results with the inclusion of this event can be found in B). A previous study has also found stronger evidence in favour of GW190521 being a second-generation BBH source and other BBH sources did not show up very strong support in favour of the second-generation sources (Kimball et al. 2021). However, we have shown in this analysis that the constraints on the GW source population parameters including GW190521 are very similar to the case without GW190521 (See B).

We consider three sets of population priors in this analysis, *Case 1*: We fix the cosmological parameters besides the Hubble constant and consider only priors on the population parameters describing the BBH distribution (other cosmological parameters are kept fixed at Planck-2018 cosmology (Planck Collaboration VI 2018)), *Case 2*: we keep fixed the values of the cosmological parameters to Planck-2018 (Planck Collaboration VI 2018) and estimate the parameters that are related to the GW source population. We consider this case to infer the value of the GW source parameters assuming a fixed cosmology. Though the choice of cosmological parameters can influence the inferred values of the GW source parameters, given the current precision of the cosmological parameters from Planck-2018, the expected statistical error in the inferred GW source parameters is much larger than the systematic error due to different choices in the value of $H_0 = 66.9$ km/s/Mpc (Planck Collaboration VI 2018) or $H_0 = 73$ km/s/Mpc (Riess et al. 2022). *Case 3*: as Case 2 but keeping the value of the delay time power-law index fixed and equal to $d = -1$, which is usually assumed as a fiducial scenario for flat in the log-space distribution of the separation between the binaries.

The analysis for Case 3 (with a fixed value of $d = -1$) is motivated to find the constraints on the parameter space for the fiducial scenario of the delay time distribution, which resembles closely previous analysis (Abbott et al. 2021b). The priors of the runs for each of the parameters can be found in Table 1. We have summarized the estimated values of the parameters for different cases in Table 2. All the quoted values of the error bars are 68 per cent confidence intervals unless mentioned otherwise.

Case 1 (GW source population + H_0): For this scenario, the joint constraints on the 13 GW source population parameters and 1 cosmological parameter, H_0, is shown in Fig. 5. The joint estimation can be broadly classified into the parameters related to the delay time + merger rate, mass distribution, and cosmology. Among the delay time + merger rate parameters, we find that data support a scenario of a steep increase in the redshift evolution of the merger rate ($d < -1$), with BBHs merger rate density at $z = 0$, $R_0 = 22.3^{+7.5}_{-5.7}{\rm Gpc}^{-3}\ {\rm yr}^{-1}$. Our constraint on the GW merger rate at high redshifts is dominated by our assumptions on the SFR and the constraints we obtain on the time delay parameters at low redshifts. However, there is a different population of BBHs that do not contribute to low redshifts according to the Madau–Dickinson SFR, but contributes to the high redshift such as the Pop-III star, which cannot be constrained from this analysis. The expected number of events after including the detector noise and duty cycle agrees well with the total number of events with SNR $\geq$ 12 considered in this analysis.

Using this model, we impose constraints on the minimum delay time distribution $t_d^{\rm min} < 10$ Gyrs.[4] We find the power-law index

[1] https://www.gw-openscience.org/O1/
[2] https://www.gw-openscience.org/O2/
[3] https://dcc.ligo.org/LIGO-T2000012/public

[4] Upper or lower limits are based on the 90 per cent CL

Downloaded from https://academic.oup.com/mnras/article/523/3/4539/7204644 by guest on 06 September 2024

Table 1. Summary of the hyperparameters and the priors used. The distribution $\mathcal{U}$(min, max) is just a uniform distribution between min and max for each parameter. Note that the breaking mass $M_{\rm break}(z_m)$ is implied by the choice of the other population parameters.

Delay time + merger rate parameters		
Parameter	**Description**	**Prior**
d	Spectral index for the power law of the delay time distribution.	$\mathcal{U}(-4,0)$
$t_d^{\rm min}$	Minimum time for the power law of the delay time distribution in Gyrs.	$\mathcal{U}(0.01,13)$
R_0	Value of the merger rate at $z=0$ in Gpc^{-3} yr^{-1}.	$\mathcal{U}(0,1000)$
Mass distribution parameters		
Parameter	**Description**	**Prior**
α	Spectral index for the power law of the primary mass distribution.	$\mathcal{U}(-4,12)$
β	Spectral index for the power law of the mass ratio distribution.	$\mathcal{U}(-4,12)$
$M_{\rm min}$	Minimum mass of the power-law component of the primary mass distribution in $M_\odot$.	$\mathcal{U}(2,10)$
$M_{\rm max}$	Maximum mass of the power-law component of the primary mass distribution in $M_\odot$.	$\mathcal{U}(50,200)$
$\lambda_{\rm g}$	Fraction of the model in the Gaussian component.	$\mathcal{U}(0,1)$
$M_{\rm PISN}(Z_*)$	The value of $M_{\rm PISN}$ for the metallicity value Z_* in $M_\odot$.	$\mathcal{U}(20,60)$
$\sigma_{\rm g}$	Width of the Gaussian component in the primary mass distribution in $M_\odot$.	$\mathcal{U}(0.4,10)$
δ_m	Range of mass tapering at the lower end of the mass distribution in $M_\odot$.	$\mathcal{U}(0,10)$
Cosmological parameters (Flat LCDM model)		
Parameter	**Description**	**Prior**
H_0	The Hubble constant parameter in km/s/Mpc.	67.4(fixed), $\mathcal{U}(20,150)$
Ω_m	Present-day matter density of the Universe.	0.315 (fixed)
Nuisance parameters		
Parameter	**Description**	**Prior**
$\alpha_{\rm Z}$	The parameter that captures a weak logarithmic dependence of $M_{\rm PISN}$ on the metallicity.	$\mathcal{U}(-15,15)$
$\gamma_{\rm Z}$	The parameter that captures the redshift dependence of the metallicity.	$\mathcal{U}(-5,0)$
ζ	The parameter that captures the metallicity at redshift $z=0$.	0.01 (fixed)

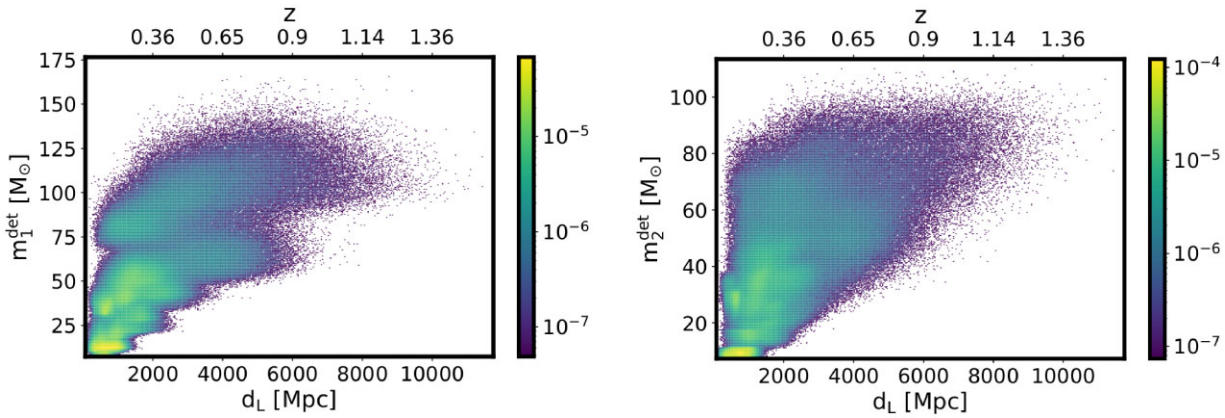

Figure 4. Two-dimensional plots of the detector frame masses and distance posterior samples for all GW events with $SNR \geq 12$. In the colour bar, the probability in the logarithmic scale can be seen. Top plot: samples of the heavy component m_1^{det}. Bottom plot: samples of the light component m_2^{det}.

of the delay time distribution to be constrained $d < -0.7$ and there is a mild preference towards values lower than $d = -1$ as expected from a simple scenario of flat in the log-space distribution of object separation of the binaries. This measurement shows a steep distribution of the delay time and hints towards scenario formation channels having less probability of a large delay time. The constraints on the $t_d^{\rm min}$ and d obtained here are driven by the joint estimation of the merger rate and mass distribution of the BBHs. Larger (smaller) values of $t_d^{\rm min}$ or larger (smaller) values of d support higher (lower) delay time values in $P(t_d)$. Mergers of BBH from higher redshifts are supported from the scenarios with large values of $t_d^{\rm min}$ or large values of d. The BBHs with heavier component masses in the data are fitted with BHs appearing from a higher redshift with higher PISN masses and a non-zero value of the delay time.

In our analysis, we also constrain models with a metallicity evolution in the Universe through the parameter γ_Z. The value of the parameter $-\gamma_{\rm Z} = 3.2^{+1.1}_{-1.2}$[5] shows that there is likely an evolution of the metallicity of the parent stars. In comparison to the current observations, (Mannucci et al. 2010; Krumholz & Dekel 2012; Sommariva et al. 2012; Dayal et al. 2013; Madau & Dickinson 2014) and also proposed from simulations (Genel 2016; Torrey et al. 2019), the posterior on $\gamma_{\rm Z}$ is consistent, supporting a decrease in the stellar metallicity with redshift. However, depending on the metallicity of the host galaxy, the parameter γ_Z can have additional dependence on the astrophysical property of the host galaxy (Artale et al. 2019, 2020), and hence can exhibit additional variation from the mean metallicity value of the Universe. Such effects can show up when more events are available and hence better modeling of the BBHs population will be needed.

[5]Measurements around the median are based on the 68 per cent CL

Downloaded from https://academic.oup.com/mnras/article/523/3/4539/7204644 by guest on 06 September 2024

Table 2. The median estimations of all parameters along with the 68 per cent credible levels can be seen here. Note that the table reports values also for parameters that were not constrained in the prior range. For a description of what are the constrained parameters, see the relevant result Section 4. The $N_{\rm exp}$ and $N_{\rm events}$ rows indicate the expected number of events in each case using the median value and are derived from the estimated parameters and the number of events detected above an SNR threshold from GWTC-3, respectively. The model that we find to be the most preferred one is highlighted in bold.

Parameters	Pop + H_0	Pop(d = −1)	Pop	Pop inc. GW190521	Pop with SNR≥11	High mass
R_0 [Gpc^{-3} yr^{-1}]	$22.3^{+7.5}_{-5.7}$	$27.3^{+7.4}_{-6.9}$	$23.5^{+7.3}_{-5.8}$	$23.2^{+7.2}_{-5.6}$	$23.0^{+6.5}_{-5.0}$	$24.5^{+7.2}_{-6.0}$
α	$3.2^{+1.0}_{-0.8}$	$3.4^{+1.1}_{-0.9}$	$3.4^{+1.1}_{-0.9}$	$3.0^{+0.9}_{-0.7}$	$3.5^{+1.0}_{-0.8}$	$3.7^{+0.8}_{-0.8}$
β	$1.0^{+1.2}_{-0.9}$	$1.2^{+1.1}_{-1.0}$	$1.0^{+1.2}_{-1.0}$	$0.9^{+1.2}_{-0.9}$	$1.0^{+1.2}_{-1.0}$	$1.0^{+1.1}_{-1.0}$
$M_{\rm max}$ [$M_\odot$]	129^{+44}_{-43}	131^{+48}_{-50}	127^{+46}_{-45}	144^{+37}_{-42}	128^{+45}_{-46}	85^{+58}_{-23}
$M_{\rm min}$ [$M_\odot$]	$4.9^{+1.0}_{-0.9}$	$4.8^{+0.8}_{-1.0}$	$4.9^{+0.8}_{-1.0}$	$4.8^{+1.8}_{-1.0}$	$4.9^{+0.7}_{-0.9}$	$4.7^{+0.7}_{-0.9}$
$M_{\rm PISN}(Z_*)$ [$M_\odot$]	$46.8^{+6.8}_{-7.3}$	$43.8^{+7.5}_{-6.5}$	$44.4^{+7.9}_{-6.3}$	$42.7^{+8.2}_{-6.5}$	$44.0^{+7.7}_{-6.0}$	$42.8^{+8.4}_{-8.0}$
$\sigma_{\rm g}$ [$M_\odot$]	$7.7^{+1.6}_{-3.1}$	$7.0^{+2.2}_{-3.6}$	$7.7^{+1.6}_{-2.6}$	$7.4^{+1.9}_{-3.4}$	$7.2^{+2.0}_{-3.0}$	$7.6^{+1.6}_{-2.1}$
$\lambda_{\rm g}$	$0.1^{+0.04}_{-0.03}$	$0.1^{+0.1}_{-0.03}$	$0.1^{+0.1}_{-0.03}$	$0.1^{+0.1}_{-0.03}$	$0.05^{+0.04}_{-0.03}$	$0.04^{+0.1}_{-0.02}$
$\delta_{\rm m}$ [$M_\odot$]	$4.9^{+2.4}_{-2.6}$	$4.9^{+2.2}_{-2.5}$	$4.7^{+2.2}_{-2.5}$	$4.5^{+2.4}_{-2.6}$	$5.2^{+2.0}_{-2.1}$	$5.3^{+2.1}_{-2.4}$
H_0 [km s^{-1} Mpc^{-1}]	42^{+19}_{-12}	–	–	–	–	–
$t_{\rm d}^{\rm min}$ [Gyrs]	$2.8^{+3.7}_{-1.7}$	$0.9^{+1.2}_{-0.7}$	$1.6^{+1.1}_{-0.9}$	$1.6^{+1.1}_{-0.9}$	$1.9^{+1.4}_{-1.1}$	$1.3^{+1.2}_{-0.8}$
$-d$	$2.4^{+1.0}_{-1.1}$	–	$2.5^{+0.9}_{-1.0}$	$2.6^{+0.9}_{-1.2}$	$2.1^{+1.1}_{-1.1}$	$2.8^{+0.8}_{-1.0}$
$-\gamma_{\rm Z}$	$3.2^{+1.1}_{-1.2}$	$2.5^{+1.3}_{-0.9}$	$2.3^{+1.4}_{-1.0}$	$3.0^{+1.2}_{-1.1}$	$2.2^{+1.3}_{-0.9}$	$2.1^{+1.3}_{-1.0}$
$\alpha_{\rm Z}$	$9.9^{+3.1}_{-3.4}$	$7.9^{+3.7}_{-3.1}$	$7.0^{+4.0}_{-2.9}$	$8.2^{+3.7}_{-2.8}$	$6.8^{+3.7}_{-2.9}$	$7.1^{+4.5}_{-3.6}$
$N_{\rm exp}$	34^{+5}_{-5}	34^{+5}_{-5}	33^{+5}_{-4}	35^{+6}_{-4}	41^{+6}_{-5}	35^{+5}_{-5}
$N_{\rm events}$	34	34	34	35	41	34

The parameters related to the mass distribution are also constrained well using a model. We have obtained a value of the power-law index of the mass distribution $\alpha = 3.2^{+1.0}_{-0.8}$ and $\beta = 1.0^{+1.2}_{-0.9}$. We also find support for a feature over a simple power law in the mass spectrum of BBH mergers with a relative height of the feature with respect to the power-law component of $\lambda_g < 0.13$ and the position of the feature is inherited at a fiducial metallicity from $M_{\rm PISN}(Z_*) = 46.8^{+6.8}_{-7.3}{\rm M}_\odot$ at $Z_* = 10^{-4}$. Differently from Abbott et al. (2021b), we are not able to exclude with confidence the value $\lambda_g = 0$ (absence of a peak feature). This is due to the use of selection criteria based on a higher SNR cut instead of an IFAR cut. We verified that with a vanilla PLP model and an IFAR cut of 1 yr as in Abbott et al. (2021b), we can exclude the absence of the peak.

The position of the peak agrees with the theoretically predicted position of the PISN mass-scale between 45 and 60 $M_\odot$ (Farmer et al. 2019a; Renzo et al. 2020; Baxter et al. 2021). As we can see from the figure, the PISN mass-scale between 45 and 60 $M_\odot$ is translated to a BBH merger excess at around 35 $M_\odot$ for $z < 0.2$. This is compatible with the overdensity of BBHs observed by the LVK in Abbott et al. (2021b). However, as redshift increases this moves to higher masses and appears to become more prominent.

For high-mass BBH, we see a significant increase in merger rate with redshift, clearly indicating that there is support for a higher merger rate from high masses at higher redshift in comparison to the low redshift. The posterior distribution of the $M_{\rm PISN}$ parameter is shown separately in Fig. 11 (bottom, blue curve). The PISN mass-scale depends on the value of metallicity and this value of $M_{\rm PISN}$ is defined in our analysis at the value of $Z_* = 10^{-4}$, which is in agreement with the parameters chosen in the simulation by Farmer et al. (2019a). The dependence of the PISN mass-scale on metallicity is stronger, i.e. the probable values of α_Z are larger, in this model than is expected from the 1-D stellar evolution models of Paxton et al. (2011, 2019).

Also, as it is evident from Fig. 5, the data have strongly suppressed any negative values of α_Z. So, scenarios of a decrease in the PISN mass-scale with a decrease in the metallicity are strongly ruled out.

It is important to note that the current theoretical estimation on the dependence of the PISN mass-scale is subject to the assumption of the stellar wind models and 1-D stellar evolution code MESA (Paxton et al. 2011, 2019). To explain the current LVK observation of the GWTC-3 by a first-generation BBH formation scenario, one needs a stronger dependence of the PISN mass-scale on the stellar metallicity and higher merger rate of the high mass BHs at high redshift. However, in the future with a higher number of sources, a better understanding of the formation channel of the BBHs will be possible.

Previously redshift dependence of different phenomenological models of BBH mass distribution was explored from GWTC-2 (Fishbach et al. 2021). They found strong evidence for the redshift evolution of the mass model when considering a truncated power law with a sharp cut-off at high masses. However, the data were consistent with both an evolving and a non-evolving mass distribution when they considered a broken power-law model as a mass model. Those findings are broadly in agreement with our results.

We find that most of the parameters do not show up significant deviation from previous results (Abbott et al. 2021b,d). However, differently from Abbott et al. (2021b,d), σ_g is not well constrained. The high σ_g estimation is an indication that there may not be a Gaussian feature in the mass distribution and the mass distribution can be smeared with an extended distribution in the masses at the higher end.

Finally, a weak measurement of the Hubble constant $H_0 = 42^{+19}_{-12}$ km/s/Mpc is made, which is in the agreement with the values from Planck-2018 (Planck Collaboration VI 2018) and SH0ES (Riess

Downloaded from https://academic.oup.com/mnras/article/523/3/4539/7204644 by guest on 06 September 2024

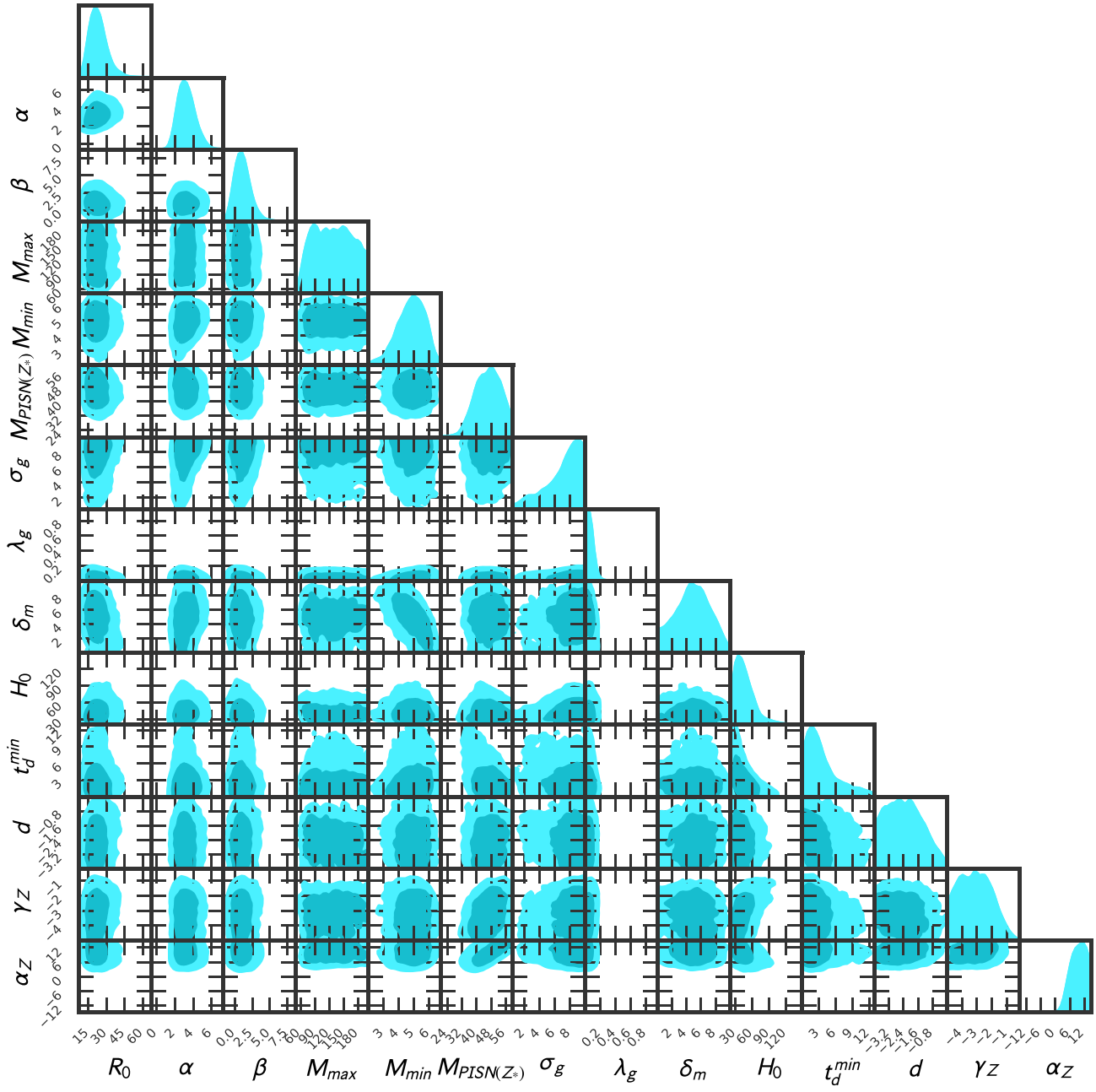

Figure 5. Posterior distributions for all the hyperparameters. Here we have fixed all cosmological parameters besides H_0 in Planck-2018 cosmology. We have used all GW events with $SNR \geq 12$. This plot corresponds to case 1 mentioned in the results section.

et al. 2022) due to large uncertainty in the current measurements. However, note the correlation between the Hubble constant and the $t_d^{\rm min}$ parameter in Fig. 5. This indicates that not being able to correctly infer the PISN mass-scale and the value of $t_d^{\rm min}$ can lead to an incorrect inference of the cosmological parameters (Mukherjee 2022).

Case 2 (main model): In this case, we only focus on the GW source population keeping the value of cosmological parameters fixed at the Planck-2018 (Planck Collaboration VI 2018). The corresponding joint estimations of the parameters are shown in Fig. 6. From the posteriors, we can obtain the merger rate model for various samples, along with the median. This can be seen in Fig. 7. We find that the value of the $M_{\rm PISN}(Z_*) = 44.4^{+7.9}_{-6.3}{\rm M}_\odot$ has moved to lower values with respect to the value allowing H_0 to vary. The value of $t_d^{\rm min}$ shows a maximum a posteriori around 1.5 Gyrs and a significantly narrower posterior with respect to *Case 1*. The posteriors for $t_d^{\rm min}$ and d are consistent with the case of varying H_0. We also find $d < -0.87$ for this case. We retrieve weak evidence of $\rm M_{PISN}(z)$ evolving with redshift as the α_Z parameter supports positive values. The value of $M_{PISN}(z)$ spans from around 30 $\rm M_\odot$ for $z = 0$ up to around 40 $\rm M_\odot$ for $z = 1$. As shown in Fig. 8, the redshift evolution of the PISN mass-scale shows a weak variation over the redshift range $z \in [0, 1]$. However, more observation will be required to confidently make any detection of the redshift evolution of PISN mass distribution. A few samples in Fig. 8 show $\rm M_{PISN}(z)$ values around 80 $\rm M_\odot$ at redshift $z = 0$ and exhibit a decrease in the $\rm M_{PISN}(z)$ with redshift evolution. Those arise from the tail of the posterior distribution due to statistical

Downloaded from https://academic.oup.com/mnras/article/523/3/4539/7204644 by guest on 06 September 2024

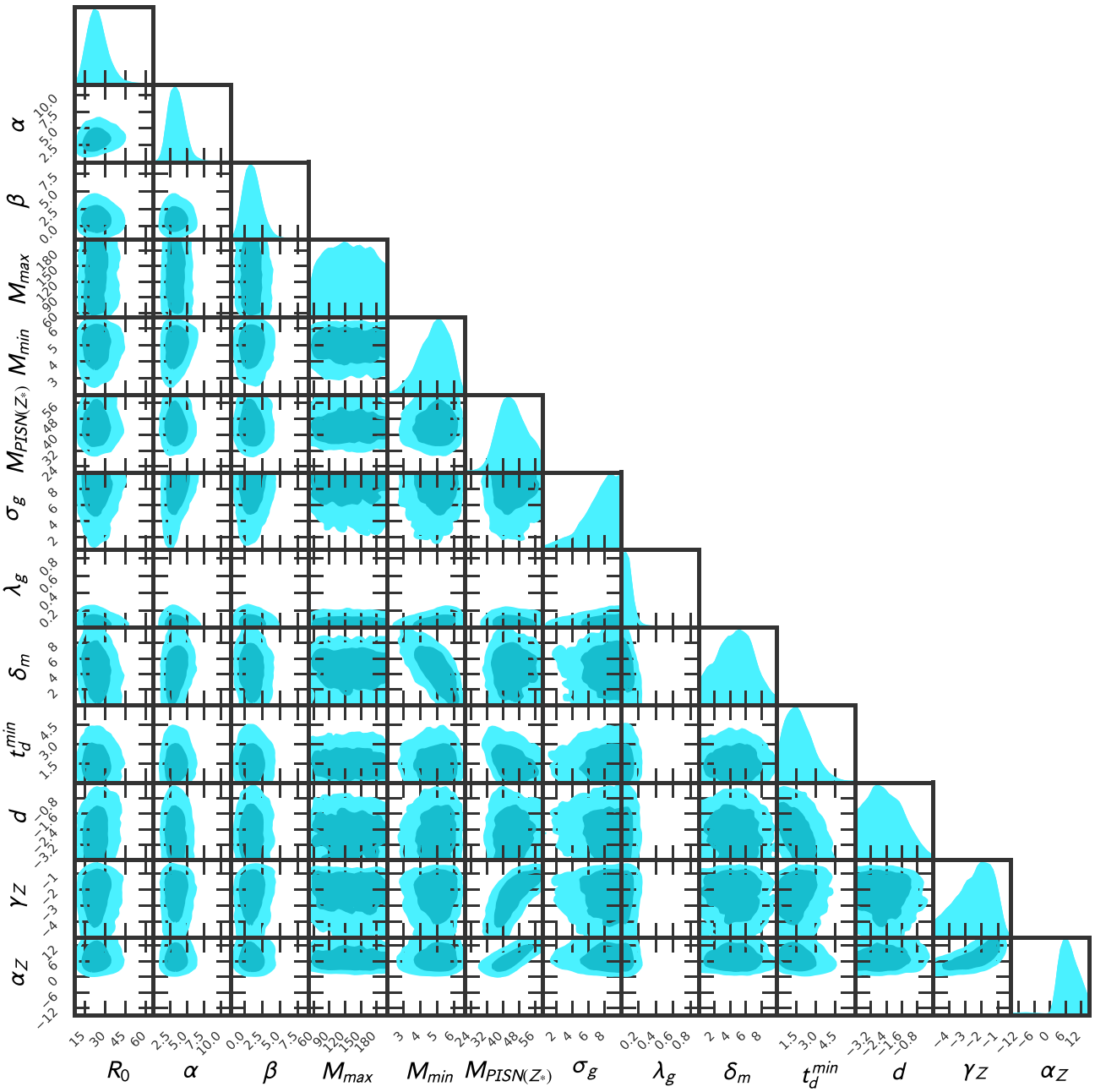

Figure 6. Posterior distributions for all the hyperparameters. Here we have fixed all cosmological parameters at Planck-2018 cosmology. We have used all GW events with $SNR \geq 12$. This plot corresponds to case 2 mentioned in the results section.

fluctuations. In Fig. 9, we show the PISN position is translated to the BBH merger primary mass spectrum when taking into account the full-time delay model.

In comparison of the simple PLG peak model with our model, we retrieve a Bayes factor ($BF_{PLG/main\,model}$) equal to $\log_{10}(BF_{PLG/main\,model}) = 0.32$ in favour of the simple PLG peak model. So, we conclude that there is a slight but insignificant preference for the PLG model. A higher number of detections is required to obtain decisive evidence for or against the redshift evolution of the BBH mass distribution.

We also compare the results with the events from GWTC-3 with SNR $\geq$ 11 in Fig. A1 (shown in the appendix). The results are consistent with the measurement of the parameters made with events having an SNR $\geq$ 12. In this analysis, we have not considered the GW event GW190521 (Abbott et al. 2020a), which has a much higher value of the component masses. Results including GW190521 can be seen in the appendix (see in Fig. B1). Constraints on the GW source parameters are very similar for both with or without GW190521.

To explore whether the model struggles to fit high masses seen in the data, we also consider a variation of our main model. We refer to this modification as the 'High mass' model and in this we impose the window function W_{t_d} only in the Gaussian peak of the distribution, leaving the power law intact. For a given redshift, we can fit higher mass events with respect to our main model. However, this model is not physically motivated within the framework of mixing BBHs scenarios. The posteriors we obtained for the high mass model can be seen in the appendix (see in Fig. C2) and are broadly consistent

Downloaded from https://academic.oup.com/mnras/article/523/3/4539/7204644 by guest on 06 September 2024

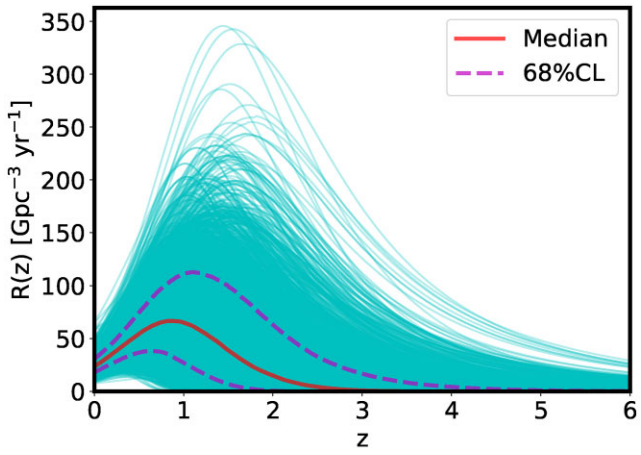

Figure 7. The merger rate evolution as a function of redshift for different posterior samples(cyan curves) of the various parameters. In the same plot, the median (red solid curve) and the 68 per cent credible levels (purple dashed curves) can also be seen. The cases with a fixed value are shown with the fixed mean value and zero uncertainty.

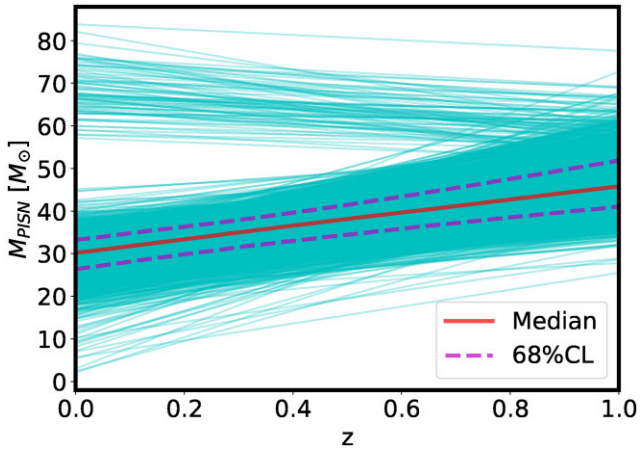

Figure 8. The $M_{\rm PISN}$ position as a function of redshift for different posterior samples (cyan curves). In the same plot, the median (red solid curve) and the 68 per cent credible levels (purple dashed curves) can also be seen.

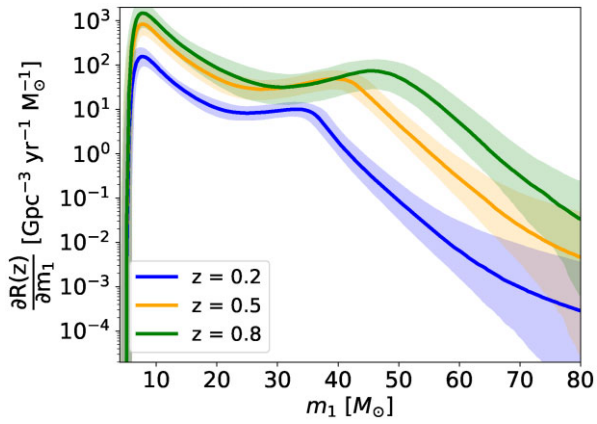

Figure 9. Differential merger rate of BBHs over primary mass as a function of redshift. The different colours indicate the merger rates at different redshifts. Solid lines show the median of the distribution, whereas the shades indicate the 68 per cent CL.

with the results obtained for our default model. Moreover, the value of the Bayes Factor in favour of our baseline model with respect to this 'high mass' model is $\log_{10}(\mathrm{BF}_{\rm main\,model/High\,mass}) = 0.17$. This implies that both models fit the data equally with a slight preference in favour of the baseline model. In Appendix C, we provide more details about this comparison.

Case 3 (GW source population (with fixed $d = -1$) parameters): In *Case 1* and *Case 2*, we have seen a value of the power-law index significantly away from $d = -1$ (usually considered as a fiducial value (Fishbach & Kalogera 2021; Mukherjee & Silk 2021)), which is possible for scenarios with flat in log-space distribution of the separation between the BHs. Here we perform a joint estimation with the value of the power-law index fixed at $d = -1$. The corresponding joint estimations of the parameters are shown in Fig. 10. For this case, the merger rate normalization is $R_0 = 27.3^{+7.4}_{-6.5}\mathrm{Gpc}^{-3}\ \mathrm{yr}^{-1}$, and the constraints on the minimum delay time $t_d^{\rm min}$ have been reduced (though completely in agreement with the value obtained with d varying from the two previous cases). This happens because, for a scenario with a fixed value of the parameter $d = -1$, the peak of the merger rate distribution is shifted towards a lower redshift; as a result by allowing a smaller value of the delay time $t_d^{\rm min}$, the peak of the merger rate position shifts towards a higher redshift. The position of the Gaussian peak has a very similar value $M_{\rm PISN}(Z_*) = 43.8^{+7.5}_{-6.5}\mathrm{M}_\odot$ with respect to the previous results of *Case 2*.

Among all our time delay models, we find that the preferred model is *Case 2*, namely the case in which cosmology is fixed but the index of the time delay distribution d varies. More interestingly, the *Case-3* model ($d = -1$) is disfavoured with respect to that of *Case 2* by a Bayes factor of $\log_{10}(\mathrm{BF}_{\rm vary\,d/fixed\,d}) = 0.38$. However, this is not enough to claim any statistical evidence and we cannot conclude any preference towards against or in favour of $d = -1$. The posteriors of t_d^{min} and $M_{\rm PISN}(Z_*)$ can be seen in the top and bottom panels of Fig. 11 for the three main cases that we considered.

The results obtained using our model including the delay time distribution and redshift evolution in the merger rate indicate a value of $\mathrm{M}_{\rm PISN} = 44.4^{+7.9}_{-6.3}$. In this model, the heavy mass BHs are formed from the low metallicity parent stars at a high redshift that has merged at a low redshift due to a delay time distribution function, which allows large values of time delay. The Bayes factor in favour of this model in comparison to the phenomenological model of PLG is comparable and cannot be well distinguished at this stage. However, in the future with more data, we will likely be able to distinguish between different scenarios.

One of the major drawbacks of the baseline model considered here is that it only considers first-generation BBHs and not the scenarios where the second-generation BBHs are present. As a result, the presence of heavier masses observed in GWTC-3 is expected to arise from stars with low metallicity. However, in reality, there can be second-generation BBHs that can contribute to the observed population. A successful physics-driven model needs to consider this aspect as well. We will explore this in a future work.

5 CONCLUSION

The mass, spin, and merger rate of BBHs are a direct probe to infer their formation channels. Though the information available from observations of BBH component spins is limited (see e.g. Abbott et al. (2021b)), we can infer the masses and luminosity distance of several BBHs using the network of LIGO/Virgo detectors. The mass distribution and merger rate of the BBHs are likely to exhibit a redshift dependence due to the dependence on the stellar metallicity

Downloaded from https://academic.oup.com/mnras/article/523/3/4539/7204644 by guest on 06 September 2024

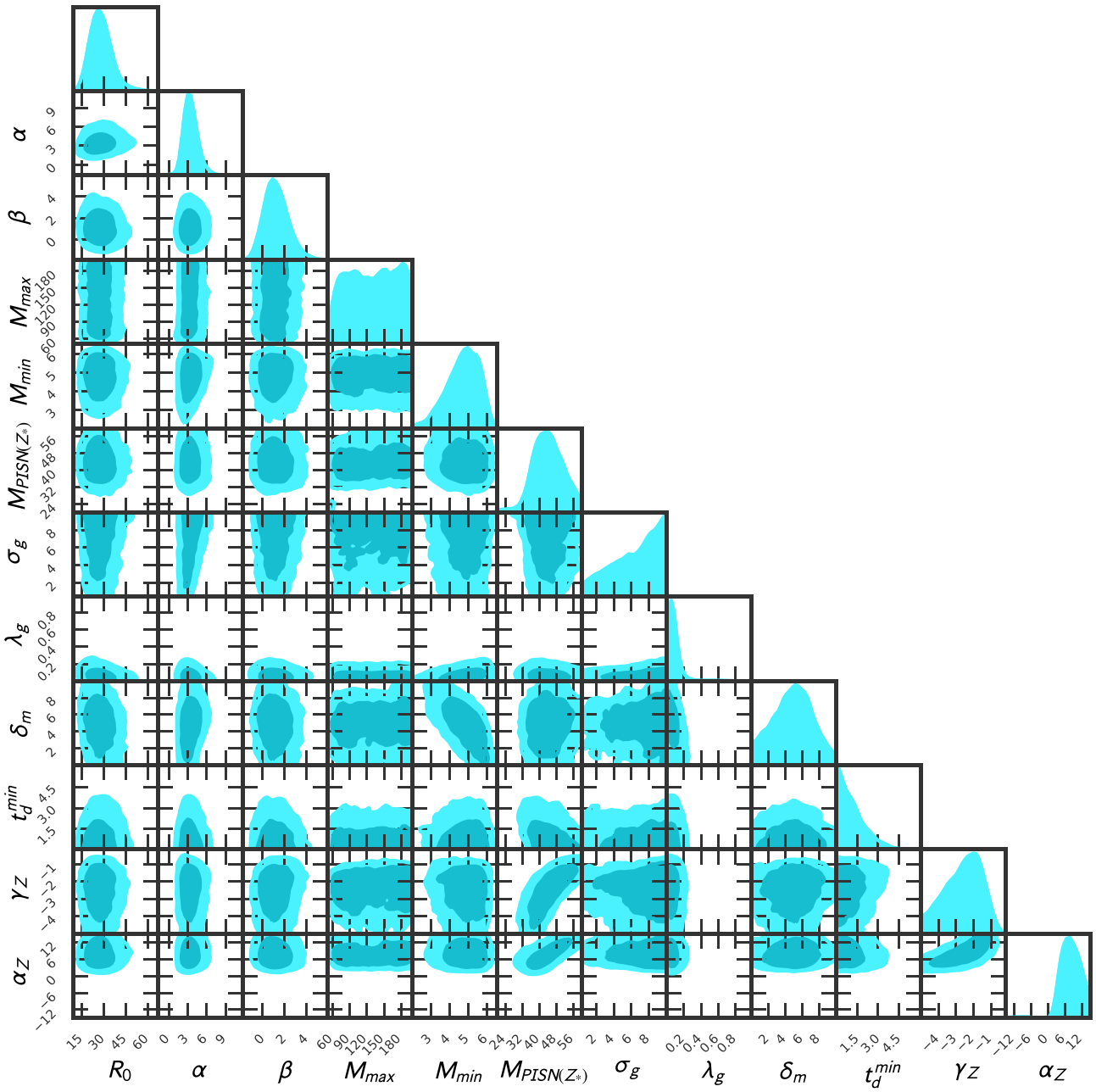

Figure 10. Posterior distributions for all the hyperparameters. Here we have fixed all cosmological parameters at Planck-2018 cosmology. We have fixed the power-law index of the delay time to $d = -1$. We have used all GW events with $SNR \geq 12$. This plot corresponds to case 3 mentioned in the results section.

and formation channel of BBHs. In this work, we consider a model that considers the redshift dependence of BBH mass distribution due to the mixing of BBHs and the redshift dependence of merger rate. We used a Bayesian analysis and estimated the values of the model's parameters using the latest GW catalogue of LVK GWTC-3.

By fitting this model with the data with both GW source parameters and cosmological parameters, we show that using a time delay distribution for BBHs and a PISN mass model in redshift, it is possible to obtain a value of $M_{\rm PISN}(Z_*)$ compatible with astrophysical expectations. This shows that the BBH excess in the mass profile of BHs could likely be reconciled with the PISN mass-scale value of around 40−50 $M_\odot$ when time delay information is considered. However, if there exist BHs of second generation that are going to have masses heavier than predicted by the PISN mass-scale, then such systems cannot be captured by this model. Though we have found that current data equally favour a model allowing only for first-generation BBH mergers with redshift-dependent mass distribution over the phenomenological redshift-independent PLG mass model. There is also an indication of the redshift dependence of the BBH mass distribution, but this trend is not statistically significant. More observations will be required to better understand the redshift dependence. Our analysis also indicates a value of $\alpha_Z = 7.0^{+4.0}_{-2.9}$ for the Case 2 (fixed H_0 case). This variation is 3−4 times larger than the typical value people expect from 1-D stellar simulations and a simplistic prescription of stellar wind models (Farmer et al. 2019b).

Downloaded from https://academic.oup.com/mnras/article/523/3/4539/7204644 by guest on 06 September 2024

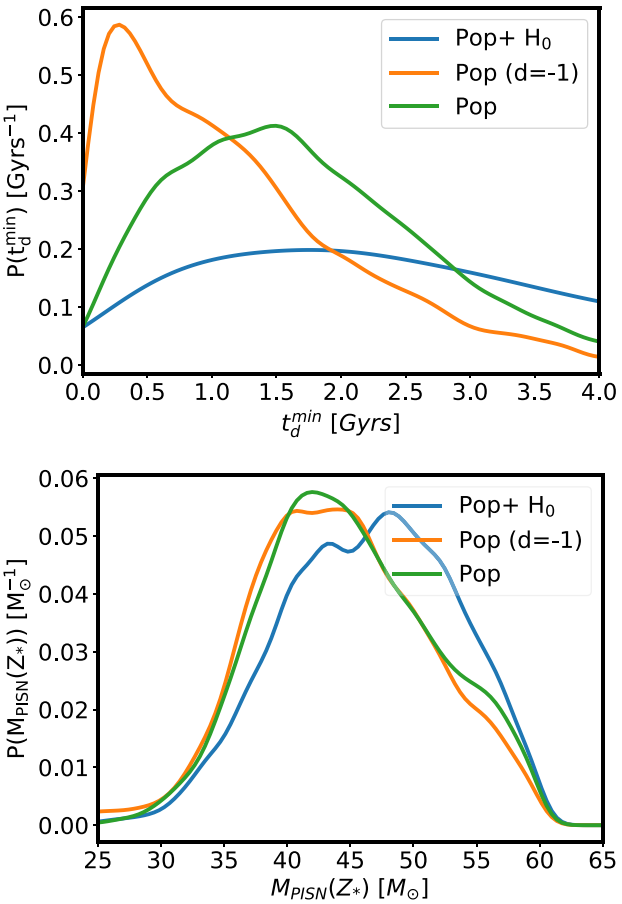

Figure 11. Posteriors on $t_d^{\min}$(top) and $M_{\rm PISN}(Z_*)$(bottom) for the three cases that we considered. Case 1: Keeping all the cosmological parameters besides H_0 fixed to Planck 2018 values and estimating H_0+population parameters (labelled as Pop + H_0). Case 2: Fix all cosmological parameters to Planck 2018 values and estimate all of the population parameters (labelled as Pop). Case 3: Keep all the cosmological parameters fixed to Planck 2018 values but also consider a fiducial fixed delay time power-law index $d = -1$ and estimate the rest of the population parameters (labelled as Pop($d = -1$)).

In the future with more data, if these results hold, then one needs to better understand the dependence of metallicity on $M_{\rm PISN}(Z_*)$.

In the hypothesis that the BBHs we consider are formed in a stellar binary scenario, we provide an upper limit for the minimum of the time delay distribution. The delay time distribution agrees with the formation channels explored in the literature. We find support for values of the power-law index of the delay time distribution $d < -1$. The value $d = -1$ is usually considered as the fiducial value for flat in log-space distribution of the spacing between the binaries. We retrieve values $d < -1$ for the power index of the time delay distribution. Though we cannot exclude with certainty the fiducial scenario $d = -1$, we do find a mild preference for smaller values.

In our analysis, we also jointly infer the value of the Hubble constant, which currently exhibits a large uncertainty and hence is consistent with the value of the Hubble constant inferred from Planck-2018 and SH0ES. However, one of the important parts is that the Hubble constant shows strong degeneracy with the GW source parameters. In particular, in this paper, we have shown that the estimation of the Hubble constant could also be impacted by the BBH time delay distribution. As a result, if the inferred value of the GW source population is incorrect, then it can bias the value of the Hubble constant and other cosmological parameter estimation.

In the future with the availability of more sources from the next observation run, a better measurement of the GW source population along with the cosmological parameters will be possible. This will shed light on the formation channels of the binary systems and the redshift dependence of the BH mass distribution. Also, improvement in the theoretical modeling will be required to capture the underlying distribution of the BBHs from both the first generation and second generations.

ACKNOWLEDGEMENTS

The authors thank Konstantin Leyde for reviewing the manuscript as a part of the LVK review process and for providing useful comments. The authors are also thankful to Thomas Dent for suggesting an interesting case (PL + G∗W) that is added in the appendix of the paper. CK is partially supported by the Spanish MINECO under the grants SEV-2016-0588 and PGC2018-101858-B-I00, some of which include ERDF funds from the European Union. IFAE is partially funded by the CERCA program of the Generalitat de Catalunya. SM is supported by the Simons Foundation. Research at Perimeter Institute is supported in part by the Government of Canada through the Department of Innovation, Science and Economic Development and by the Province of Ontario through the Ministry of Colleges and Universities. SM is supported by the ANR COSMERGE project, grant ANR-20-CE31-001 of the French Agence Nationale de la Recherche. This analysis is carried out at the computing facility of the LSC cluster. We acknowledge the use of the following packages in this work: Astropy (Astropy Collaboration et al. 2013, 2018), BILBY (Ashton et al. 2019), Giant-Triangle-Confusogram (Bocquet & Carter 2016), IPython (Pérez & Granger 2007), Matplotlib (Hunter 2007), NumPy (van der Walt, Colbert & Varoquaux 2011), and SciPy (Jones et al. 01). The authors are grateful for computational resources provided by the LIGO Laboratory and supported by National Science Foundation Grants PHY-0757058 and PHY-0823459. The authors would like to thank the LIGO/Virgo/KAGRA scientific collaboration for providing the data. LIGO is funded by the U.S. National Science Foundation. Virgo is funded by the French Centre National de Recherche Scientifique (CNRS), the Italian Istituto Nazionale della Fisica Nucleare (INFN), and the Dutch Nikhef, with contributions by Polish and Hungarian institutes. This material is based upon work supported by NSF's LIGO Laboratory, which is a major facility fully funded by the National Science Foundation.

DATA AVAILABILITY

The data underlying this article are available on this website https://www.gw-openscience.org.

REFERENCES

Aasi J. et al., 2015, Class. Quant. Grav., 32, 074001
Abbott B. P. et al., 2016a, Phys. Rev. D, 93, 112004
Abbott B. P. et al., 2016b, Phys. Rev. Lett., 116, 131103
Abbott B. P. et al., 2018, Living Rev. Rel., 21, 3
Abbott B. et al., 2019a, Phys. Rev. X, 9
Abbott B. P. et al., 2019b, Astrophys. J., 882, L24
Abbott R. et al., 2020a, Phys. Rev. Lett., 125, 101102
Abbott R. et al., 2020b, Astrophys. J., 896, L44
Abbott R. et al., 2021d, preprint (https://arxiv.org/abs/2111.03604)
Abbott R. et al., 2021a, preprint(arXiv: 2108.01045)
Abbott R. et al., 2021c, preprint (arXiv:2111.03606)

Downloaded from https://academic.oup.com/mnras/article/523/3/4539/7204644 by guest on 06 September 2024

Abbott R. et al., 2021b, preprint (arXiv:2111.03634)
Abbott R. et al., 2021e, Phys. Rev. X, 11, 021053
Abbott R. et al., 2021f, SoftX, 13, 100658
Abbott B. P. et al., 2021g, Astrophys.J., 909, 218
Abbott R. et al., 2021h, Astrophys. J. Lett., 913, L7
Acernese F. et al., 2014, Class. Quantum Gravity, 32, 024001
Planck Collaboration VI, 2018,, AA, 641, 46
Akutsu T. et al., 2021, Prog. Theor. Exp. Phys., 221, 05A101
Arabsalmani M., Sahni V., Saini T. D., 2013, Phys. Rev. D, 87, 083001
Artale M. C., Mapelli M., Giacobbo N., Sabha N. B., Spera M., Santoliquido F., Bressan A., 2019, MNRAS, 487, 1675
Artale M. C., Mapelli M., Bouffanais Y., Giacobbo N., Spera M., Pasquato M., 2020, MNRAS, 491, 3419
Ashton G. et al., 2019, Astrophys. J. Suppl., 241, 27
Aso Y., Michimura Y., Somiya K., Ando M., Miyakawa O., Sekiguchi T., Tatsumi D., Yamamoto H., 2013, Phys. Rev. D, 88, 043007
Astropy Collaboration et al., 2013, A&A, 558, A33
Astropy Collaboration et al., 2018, AJ, 156, 123
Banerjee S., Baumgardt H., Kroupa P., 2010, MNRAS, 402, 371
Baxter E. J., Croon D., McDermott S. D., Sakstein J., 2021, Astrophys. J. Lett., 916, L16
Belczynski K., Kalogera V., Bulik T., 2002, ApJ, 572, 407
Bera S., Rana D., More S., Bose S., 2020, Astrophys. J., 902, 79
Bethe H. A., Brown G. E., 1998, Astrophys. J., 506, 780
Bocquet S., Carter F. W., 2016, J. Open Source Softw., 1,46
Buikema A. et al., 2020, Phys. Rev. D, 102, 062003
du Buisson L. et al., 2020, MNRAS, 499, 5941
Cañas-Herrera G., Contigiani O., Vardanyan V., 2021, ApJ, 918, 20
Cao L., Lu Y., Zhao Y., 2018, MNRAS, 474, 4997
Cigarrán Díaz C., Mukherjee S., 2022, MNRAS, 511, 2782
Dayal P., Ferrara A., Dunlop J. S., 2013, MNRAS, 430, 2891
Del Pozzo W., 2012, Phys. Rev. D, 86, 043011
Ding X., Biesiada M., Zheng X., Liao K., Li Z., Zhu Z.-H., 2019, JCAP, 2019, 033
Dominik M., Belczynski K., Fryer C., Holz D. E., Berti E., Bulik T., Mandel I., O'Shaughnessy R., 2012, ApJ, 759, 52
Dominik M. et al., 2015, Astrophys. J., 806, 263
Elbert O. D., Bullock J. S., Kaplinghat M., 2018, MNRAS., 473, 1186
Eldridge J. J., Stanway E. R., Tang P. N., 2019, MNRAS., 482, 870
Ezquiaga J. M., Holz D. E., 2022, Phys. Rev. Lett., 129, 061102
Farmer R., Renzo M., de Mink S. E., Marchant P., Justham S., 2019a, ApJ, 887, 53
Farmer R., Renzo M., de Mink S. E., Marchant P., Justham S., 2019b, Astrophys. J., 887, 53
Farr W. M., Fishbach M., Ye J., Holz D., 2019, Astrophys. J. Lett., 883, L42
Finke A., Foffa S., Iacovelli F., Maggiore M., Mancarella M., 2021, J. Cosmol. Astropart. Phys., 2021, 026
Fishbach M., Kalogera V., 2021, Astrophys. J. Lett., 914, L30
Fishbach M. et al., 2019, Astrophys. J. Lett., 871, L13
Fishbach M. et al., 2021, ApJ, 912, 98
Genel S., 2016, ApJ, 822, 107
Giacobbo N., Mapelli M., Spera M., 2018, MNRAS, 474, 2959
Gray R. et al., 2020, Phys. Rev. D, 101, 122001
Gregory M. H. e. a., 2010, Class. Quantum Gravity, 27, 084006
Heger A., Woosley S. E., 2002, ApJ, 567, 532
Hunter J. D., 2007, Comput. Sci. Eng., 9, 90
Jones E., Oliphant T., Peterson P. et al., 2001, SciPy: Open source scientific tools for Python, http://www.scipy.org/
Kimball C. et al., 2021, Astrophys. J. Lett., 915, L35
Kroupa P., 2002, Science, 295, 82
Krumholz M. R., Dekel A., 2012, ApJ, 753, 16
Lamberts A., Garrison-Kimmel S., Clausen D. R., Hopkins P. F., 2016, MNRAS, 463, L31
Leandro H., Marra V., Sturani R., 2022, Phys. Rev. D, 105, 023523
Leyde K., Mastrogiovanni S., Steer D. A., Chassande-Mottin E., Karathanasis C., 2022, preprint (arXiv:2202.00025)
MacLeod C. L., Hogan C. J., 2008, Phys. Rev. D, 77, 043512
Madau P., Dickinson M., 2014, Annu. Rev. Astron. Astrophys., 52, 415
Mancarella M., Genoud-Prachex E., Maggiore M., 2022, Phys. Rev. D, 105, 064030
Mandel I., de Mink S. E., 2016, MNRAS, 458, 2634
Mandel I., Farr W. M., Gair J. R., 2019, MNRAS, 486, 1086
Mannucci F., Cresci G., Maiolino R., Marconi A., Gnerucci A., 2010, MNRAS, 408, 2115
Mapelli M., Giacobbo N., Ripamonti E., Spera M., 2017, MNRAS, 472, 2422
Mastrogiovanni S. et al., 2021a, Phys. Rev. D, 104, 062009
Mastrogiovanni S., Haegel L., Karathanasis C., Hernandez I. M. n., Steer D. A., 2021b, JCAP, 2021, 043
Mehta A. K., Buonanno A., Gair J., Miller M. C., Farag E., deBoer R. J., Wiescher M., Timmes F. X., 2022, ApJ, 924, 39
Mukherjee S., 2022, MNRAS, 515, 5495
Mukherjee S., Dizgah A. M., 2022, Astrophys. J. Lett., 937, L27
Mukherjee S., Silk J., 2021, MNRAS, 506, 3977
Mukherjee S., Wandelt B. D., 2018, preprint (arXiv:1808.06615)
Mukherjee S., Wandelt B. D., Silk J., 2020, MNRAS, 494, 1956
Mukherjee S., Wandelt B. D., Nissanke S. M., Silvestri A., 2021a, Phys. Rev. D, 103, 043520
Mukherjee S., Wandelt B. D., Silk J., 2021b, MNRAS, 502, 1136
Mukherjee S., Lavaux G., Bouchet F. R., Jasche J., Wandelt B. D., Nissanke S., Leclercq F., Hotokezaka K., 2021c, A&A, 646, A65
Mukherjee S., Krolewski A., Wandelt B. D., Silk J., 2022, preprint (arXiv:2203.03643)
O'Shaughnessy R., Kalogera V., Belczynski K., 2010, ApJ, 716, 615
Oguri M., 2016, Phys. Rev. D, 93, 083511
Palmese A., Bom C. R., Mucesh S., Hartley W. G., 2023, ApJ, 943, 56
Paxton B., Bildsten L., Dotter A., Herwig F., Lesaffre P., Timmes F., 2011, ApJS, 192, 3
Paxton B. et al., 2019, ApJS, 243, 10
Pérez F., Granger B. E., 2007, Comput. Sci. Eng., 9, 21
Portegies Zwart S. F., Yungelson L. R., 1998, A&A, 332, 173
Renzo M., Farmer R. J., Justham S., de Mink S. E., Götberg Y., Marchant P., 2020, MNRAS, 493, 4333
Riess A. G. et al., 2022, ApJL, 934, L7
Safarzadeh M., Farr W. M., 2019, ApJ, 883, L24
Santoliquido F., Mapelli M., Giacobbo N., Bouffanais Y., Artale M. C., 2021, Mon. Not. Roy. Astron. Soc., 502, 4877
Scelfo G., Boco L., Lapi A., Viel M., 2020, JCAP, 2020, 045
Scelfo G., Spinelli M., Raccanelli A., Boco L., Lapi A., Viel M., 2022, JCAP, 2022, 004
Schutz B. F., 1986, Nature, 323, 310
Soares-Santos M. et al., 2019, Astrophys. J. Lett., 876, L7
Sommariva V., Mannucci F., Cresci G., Maiolino R., Marconi A., Nagao T., Baroni A., Grazian A., 2012, A&A, 539, A136
van Son L. A. C. et al., 2022, ApJ, 931, 17
Spera M., Mapelli M., 2017, MNRAS, 470, 4739
Talbot C., Thrane E., 2018, ApJ, 856, 173
Taylor S. R., Gair J. R., Mandel I., 2012, Phys. Rev. D, 85, 023535
The LIGO Scientific Collaboration et al., 2023, preprint (arXiv:2302.03676)
Thrane E., Talbot C., 2019, Publ. Astronom. Soc. Aust., 36, e010
Toffano M., Mapelli M., Giacobbo N., Artale M. C., Ghirlanda G., 2019, MNRAS, 489, 4622
Torrey P. et al., 2019, MNRAS, 484, 5587
Tse M. et al., 2019, Phys. Rev. Lett., 123, 231107
Vitale S., Farr W. M., Ng K., Rodriguez C. L., 2019, Astrophys. J. Lett., 886, L1
Vitale S., Gerosa D., Farr W. M., Taylor S. R., 2021, in, Handbook of Gravitational Wave Astronomy. Springer Singapore, p. 1
Ye C., Fishbach M., 2021, Phys. Rev. D, 104, 043507
You Z.-Q., Zhu X.-J., Ashton G., Thrane E., Zhu Z.-H., 2021, Astrophys. J., 908, 215
van der Walt S., Colbert S. C., Varoquaux G., 2011, Comput. Sci. Eng., 13, 22

Downloaded from https://academic.oup.com/mnras/article/523/3/4539/7204644 by guest on 06 September 2024

APPENDIX A: PARAMETER ESTIMATION WITH A DIFFERENT SNR THRESHOLD

Here we explore the variation of our results in the case of a lower SNR threshold. In addition to the GW events that we used with SNR $\geq$ 12 (see Section 4), we are now using additionally all events with SNR $\geq$ 11. Lowering the SNR causes to run the analysis with 41 events in total. The different posteriors can be seen in Fig. A1. It is apparent that all of the posteriors are in agreement with the *SNR* $\geq$ 12 results. The only noticeable difference can be seen in the posterior of the time delay's distribution power-law index d. We see that the peak of the posterior has moved to slightly higher values, though the posterior is fully in agreement with the SNR $\geq$ 12 one. The calculated expected value of the events is $N_{\rm exp} = 41^{+6}_{-5}$ and agrees with the 41 events that were used.

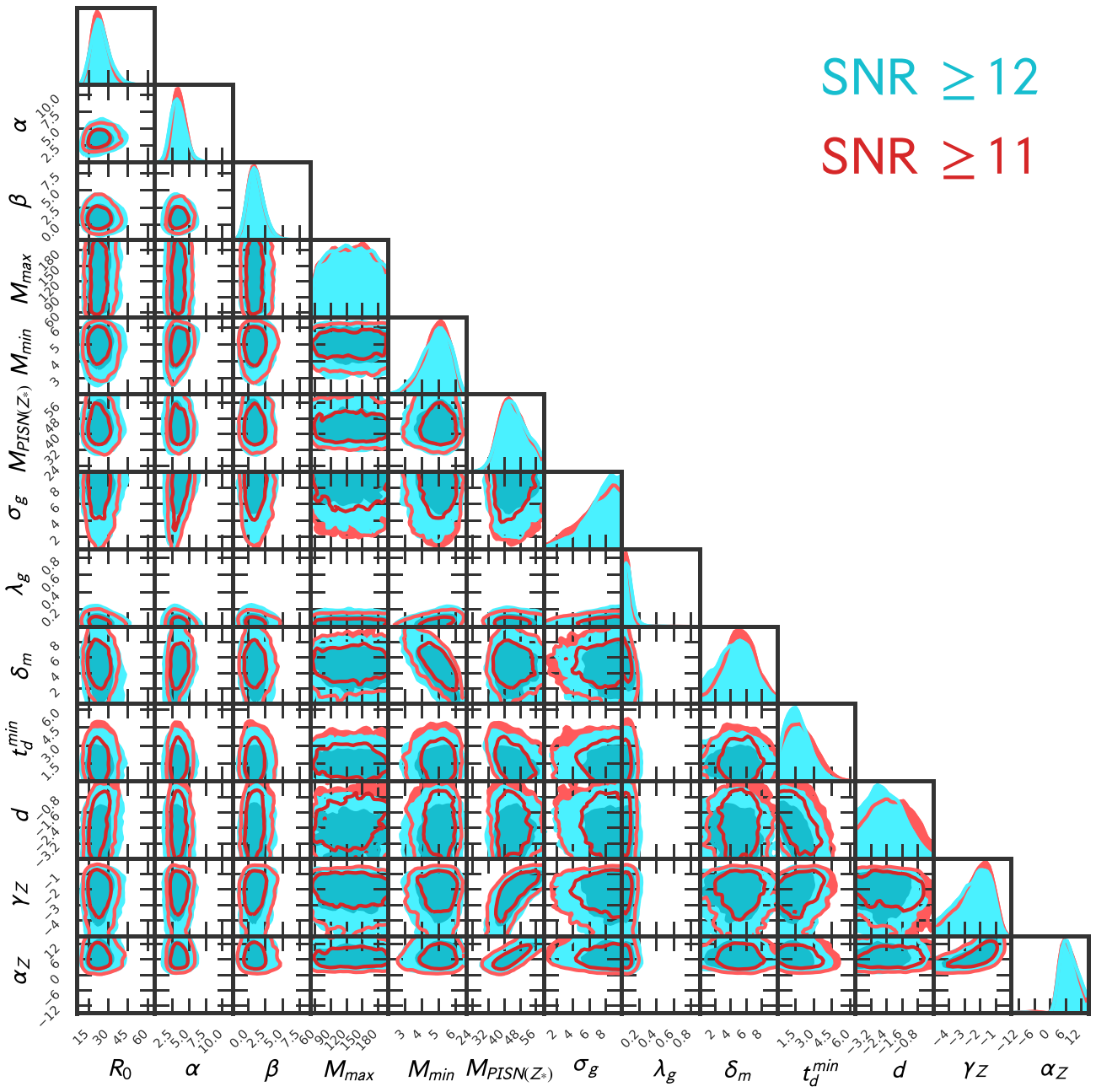

Figure A1. Posterior distributions for all the hyperparameters. Here we have fixed all cosmological parameters at Planck-2018 cosmology. Different posteriors for different SNR thresholds can be seen.

Downloaded from https://academic.oup.com/mnras/article/523/3/4539/7204644 by guest on 06 September 2024

APPENDIX B: PARAMETER ESTIMATION INCLUDING GW190521

The posteriors of all parameters when including the event GW190521 can be seen in Fig. B1. Again all of the posteriors are in agreement with the ones obtained excluding GW190521. We find a slightly less steep power law for the m_1 distribution with respect to the run excluding GW190521 with a power-law index for the mass distribution of $\alpha = 3.0^{+0.9}_{-0.7}$. We also retrieve a flatter σ_g posterior and a posterior for $M_{\rm max}$ that disfavours smaller values of masses, though fully in agreement with the previous results. These differences are because GW190521 components are very massive. For the model to fit the extra support at high masses, it needs a less steep power-law index for the mass distribution. At the same time, this leads to a less wide Gaussian peak and to the fact that small values of $M_{\rm max}$ are now disfavoured. We also recover some minor changes in the posteriors for d, α_Z, and γ_Z. We estimate that the expected number of events is $N_{\rm exp} = 35^{+6}_{-5}$, which matches the 35 events used.

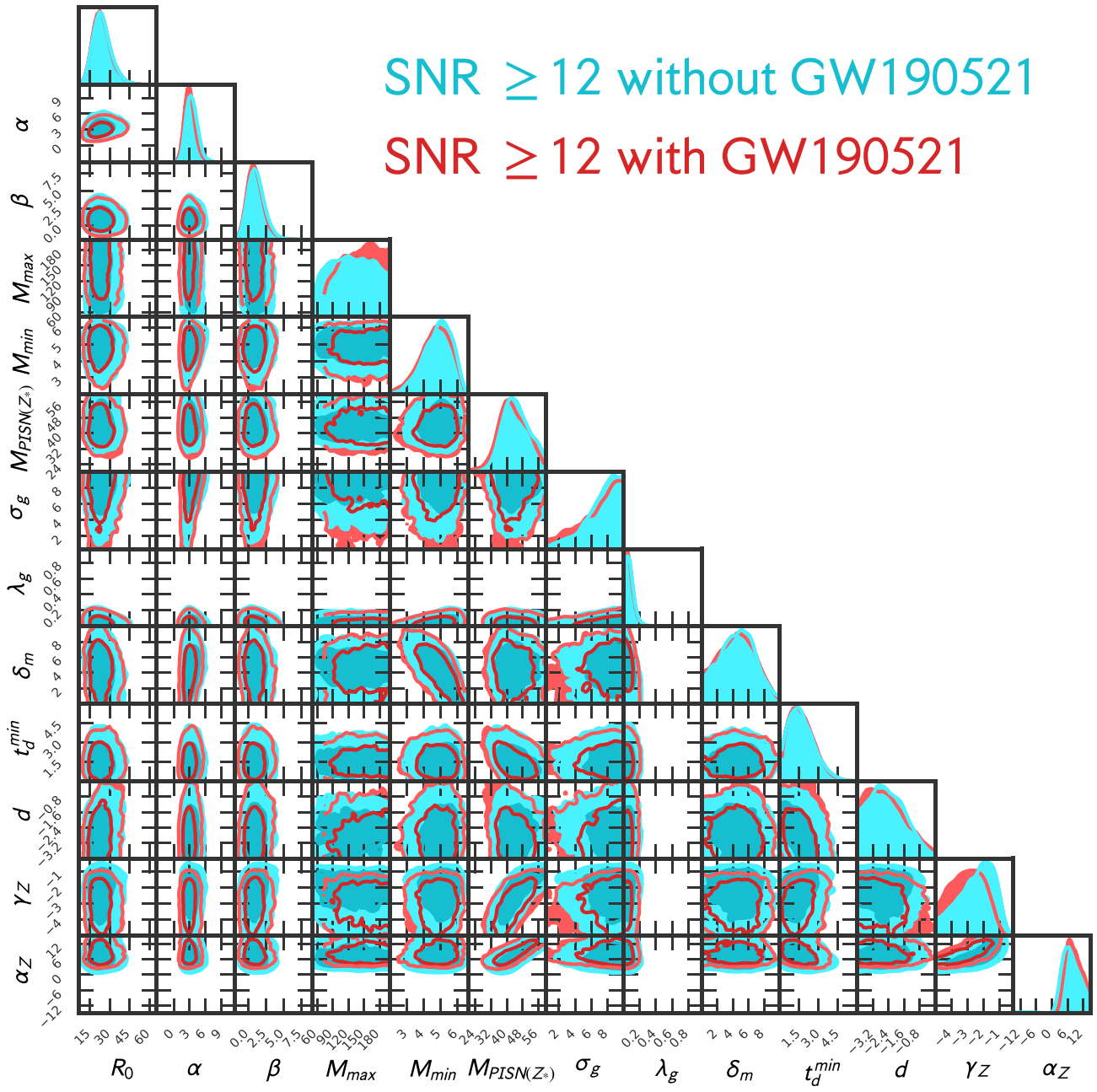

Figure B1. Posterior distributions for all the hyperparameters. Here we have fixed all cosmological parameters at Planck-2018 cosmology. Different posteriors including or excluding GW190521 can be seen.

Downloaded from https://academic.oup.com/mnras/article/523/3/4539/7204644 by guest on 06 September 2024

APPENDIX C: HIGH MASS MODEL

Here we employ a new model to be able to fit higher masses and we refer to it as the high mass model. Instead of imposing the window function W_{t_d} to the PLG peak, we instead leave the power law intact and only impose the windowing to the Gaussian peak of the distribution (see Fig. C1). The posteriors obtained by this model can be seen in Fig. C2. It is apparent that most of the posteriors are in agreement with those obtained by the usual model. However, the posterior for $M_{\rm max}$ seems to give more stringent constraints in this case, with high values of masses being disfavoured. This is expected since in this model the power law is left intact allowing for significant support for higher values in the mass distribution after the $M_{\rm PISN}$. Therefore, because we do not have posterior samples in these ranges of masses, the Bayesian inference can exclude the very high mass values. This does not affect our estimations for the time delay parameters, since the posteriors are in agreement with those from our main model.

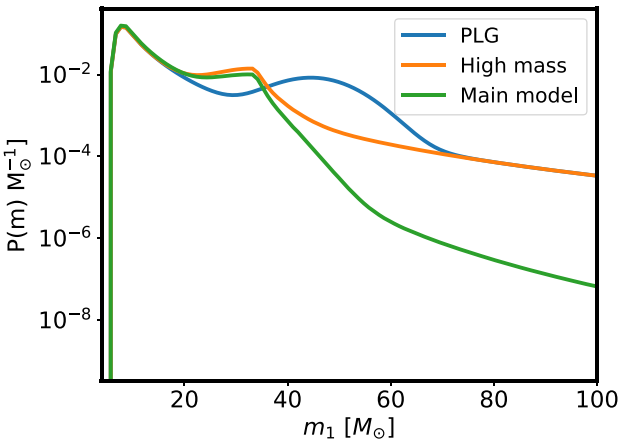

Figure C1. Comparison of the m_1 distribution for different mass models. For the values of parameters, we selected the median values of our estimations from *Case 2* at $z_m = 0.1$.

Downloaded from https://academic.oup.com/mnras/article/523/3/4539/7204644 by guest on 06 September 2024

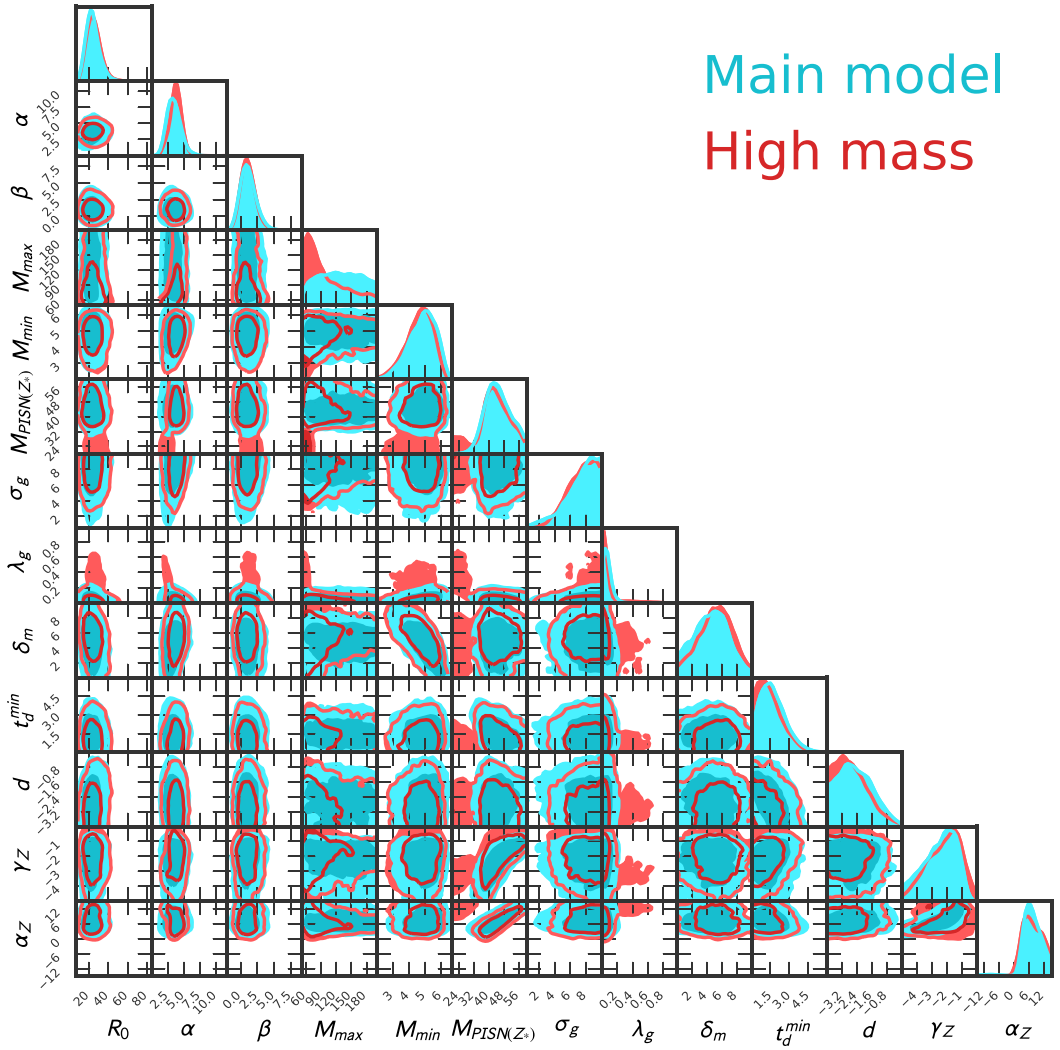

Figure C2. Posterior distributions for all the hyperparameters. Here we have fixed all cosmological parameters at Planck-2018 cosmology. The posteriors for the high mass model can be seen, as well as the posteriors obtained for the usual model.

This paper has been typeset from a TEX/LATEX file prepared by the author.

Downloaded from https://academic.oup.com/mnras/article/523/3/4539/7204644 by guest on 06 September 2024

© 2023 The Author(s)
Published by Oxford University Press on behalf of Royal Astronomical Society